Tectonophysics 612–613 (2014) 1–17

Contents lists available at ScienceDirect

Tectonophysics

journal homepage: www.elsevier.com/locate/tecto

Fault network modeling of crustal deformation in California constrained using GPS and geologic observations☆

Yuehua Zeng [a,*], Zheng-Kang Shen [b,c]

[a] US Geological Survey, Golden, CO, United States
[b] Department of Earth and Space Sciences, University of California, Los Angeles, United States
[c] School of Earth and Space Sciences, Peking University, Beijing, China

ARTICLE INFO

Article history:
Received 13 June 2012
Received in revised form 13 November 2013
Accepted 22 November 2013
Available online 1 December 2013

Keywords:
Kinematic fault model
GPS observations
Crustal deformation
Fault slip rate

ABSTRACT

We have developed a kinematic fault network model of crustal deformation in an elastic half-space. Surface deformation is calculated using this model assuming each fault segment slipping beneath a locking depth. Each fault segment connects to its adjacent elements with slip vector continuity imposed at fault nodes or intersections; the degree of the constraints determines whether deformation is block-like or not. We apply this model to invert GPS observations for slip rates on major faults in California with geological rate constraints. Based on the F-test result, we find that lesser block-like models fit the data significantly better than the strictly block-like model. Our final inversion shows a slip rate varying from 20 to 23 mm/yr along the northern San Andreas from the Santa Cruz to the North Coast segment. Slip rates vary from 9 to 13 mm/yr along the Hayward to the Maacama fault segment, and from 15 to 3 mm/yr along the central Calaveras to the West Napa fault segment. For the central California Creeping Zone, the result suggests a depth dependent creep rate with an average of 22 mm/yr over the top 5 km and 32 mm/yr underneath. From the Mojave to San Bernardino Mountain segments, we also find a significant decrease in slip rate along the San Andreas in comparison with the geologic rates, in contrast to a significant increase in slip rate on faults along the eastern California shear zone. Along the southern San Andreas, slip rates vary from 21 to 25 mm/yr from the Coachella Valley to Imperial Valley segments. Slip rates range from 0 to 3 mm/yr across the western Transverse Ranges faults, which is consistent with the regional crustal thickening. Overall slip rates derived from geodetic observations correlate strongly with the geologic slip rates statistically, suggesting high compatibility between geodetic and geologic observations.

Published by Elsevier B.V.

1. Introduction

With advances in Global Positioning System (GPS) technology, detailed crustal deformation has been surveyed over the world for the past two decades, particularly across plate boundaries and at tectonically active intra-plate regions. These data have provided the best estimates of deformation rates over years and decades, and strains accumulated and released before, during, and after earthquakes over the observational time period. Those geodetic data are crucial to our understanding of earthquake processes and plate tectonics.

California and its neighboring regions are home to a major plate boundary between the Pacific and North American plates. Interactions between the two plates result in complicated fault motions along their boundary and further into the plate interiors. Most fault sections of this major boundary are locked, resulting in high stress that is eventually released in small to large earthquakes, posing significant threat to the region's large urban population. Precise GPS positioning is used to monitor plate tectonic motions and help interpret interseismic fault loading, coseismic unloading, and aseismic slip at millimeter-level precision. Analysis and modeling of geodetic signals provide fundamental data on fault slip rates and these data can give information on earthquake occurrence that eventually will lead to better seismic hazard assessment. Questions arise on how crustal deformation occurs: is it deformed elastically in a block-like form (e.g. d'Alessio et al., 2005; Meade and Hager, 2005) or in a more complex form with significant off-fault strain accumulation (Bird, 2009; McCaffrey, 2005)? By considering the block model and a completely segmented fault-based model as two end members of geodetic deformations, we want to test where the best fitting model to the GPS observations lies in between the two end members without invoking any other model complexities, such as distributed visco-elastic responses (Johnson et al., 2007; Pollitz and Schwartz, 2008; Chuang and Johnson, 2011; Hearn et al., 2013) and provide answers to the questions raised above.

In this paper, we start with a simple fault-based model that assumes deformation on the earth surface is the result of only slip along faults. We introduce a kinematic fault network model that calculates the geodetic ground deformation from any given distribution of slip rates

☆ Peer review disclaimer: This draft manuscript is distributed solely for purposes of scientific peer review. Its content is deliberative and predecisional, so it must not be disclosed or released by reviewers. Because the manuscript has not yet been approved for publication by the U.S. Geological Survey (USGS), it does not represent any official USGS finding or policy.

* Corresponding author at: US Geological Survey, BOX 25046, MS 966, CO 80225, United States.

0040-1951/$ – see front matter. Published by Elsevier B.V.
http://dx.doi.org/10.1016/j.tecto.2013.11.030

across a fault network in the area. Similar to a block model, the entire area is divided into blocks that are bounded by the fault networks. Given the dense GPS velocity observations available in California and its neighboring regions and geological slip rate constraints for many fault segments, we invert these datasets to determine slip rates on fault segments over the entire fault network. Parameters that constrain the degree of block-like motion are optimized based on the trade-off between the fit to the observation and the total number of model resolution and the results are used to determine the pattern of crust deformation. The results are also compared with slip rates based on geological measurements. Differences between the two classes of slip rates provide important insights into changes in present day tectonic motions. The results also provide critical input to earthquake rupture forecasts in the region that can be applied in seismic hazard evaluations.

2. Kinematic fault network model

The dense GPS velocity observations in California and its neighboring region provide an unprecedented opportunity to study geodetic deformations caused by fault slips on major active faults in the region. We introduce a kinematic fault network model that simulates geodetic ground deformation rates from a given distribution of slip rates across all the known major faults in the region. The correspondence between geodetic deformation and fault slip rates is uniquely determined as long as the fault network structure and the constraints on the slip variability and continuity conditions are defined between connecting fault segments. The uniqueness is guaranteed by the well-known elastic representation theory (Aki and Richards, 1980). For a given slip rate distribution on all the faults, the ground velocity vector at any point is obtained by taking a spatial convolution of the static point source Green's function with the slip rate functions over the faults:

$$\dot{u}_n(r) = \int_{-\infty}^{\infty} \mu \nu_i \Delta \dot{u}_j(\xi) \frac{\partial G_{ni}(r,\xi)}{\partial \xi_j} d\sum \tag{1}$$

where μ is the shear modulus, ν_i is a unit vector normal to the fault, $\Delta\dot{u}_j$ is the j-th component of slip rate on the fault, and G_{ni} is the Green's function calculated from receiver to source. The vector r describes the receiver location and ξ describes the corresponding source point where the Green's function is calculated.

We use Okada (1992) to calculate the surface deformation in an elastic half space. Our kinematic fault network model assumes that each fault segment slips at certain rates beneath a locking depth except at a few fault segments where shallow creep is allowed. In block deformation modeling (e.g., Meade and Hager, 2005), surface deformation is determined by block rotation and sum of elastic deformation calculated using a back-slip model at block boundaries and slip rates estimated by the relative motion across block boundaries. Using the same slip rate distribution provided by block deformation modeling, our buried fault model gives the same surface deformation as that from a block model for crustal motion analysis (e.g., McCaffrey, 2005; Meade and Hager, 2005).

We rewrite Eq. (1) in a discretized form that gives the relation between GPS ground velocities and fault slip rates, including creep rates:

$$\dot{u}_n(r_i) = \sum_{j=1}^{N} \mathrm{U}^1_{nj}\Delta\dot{u}^j_1 + \mathrm{U}^2_{nj}\Delta\dot{u}^j_2 + \sum_{k=1}^{M} \mathrm{U}^1_{cree,nk}\Delta c^k_1 + \mathrm{U}^2_{cree,nk}\Delta c^k_2 \tag{2}$$

where $\dot{u}_n$ is the predicted surface velocities, n is the component of the horizontal velocity, r_i is the location of the i-th station, $\Delta\dot{u}^j_1$ and $\Delta\dot{u}^j_2$ are the fault parallel and fault normal slip rates along the j-th fault segment, respectively, U^1_{nj} and U^2_{nj} are the Green's function relating those fault slip rates to velocities at the i-th station, Δc^k_1 and Δc^k_2 are the fault parallel and fault normal creep rates along the k-th fault segment, respectively, and $\mathrm{U}^1_{cree,nk}$ and $\mathrm{U}^2_{cree,nk}$ are the Green's function relating the fault creep rates at shallow depth to velocities at the i-th station. N is the total number of fault segments. M is the total number of creeping fault segments.

Following the same block modeling concept, we assume that all the fault segments are linked to its adjacent segments. We impose slip vector conservation at fault nodes or intersections to regulate slip variability and to simulate block-like motion. The conservation constraint at each node point is given by:

$$\frac{\alpha}{l}\sum_i \varepsilon_i \Delta\dot{u}^i = 0 \tag{3}$$

where $\varepsilon_i = 1$ if the i-th fault segment strikes towards the node, otherwise, $\varepsilon_i = -1$, α is a weighting parameter, l is the average half-length of the fault segments that connect to the node. In addition, we minimize slip rates along the fault normal direction because fault systems in the region are dominated by strike slip faults. This minimization is given by:

$$\beta\frac{\Delta\dot{u}^j_2}{l_i} = 0 \tag{4}$$

where $\Delta\dot{u}^j_2$ is the fault normal slip rate along the i-th fault segment, l_i is the i-th fault segment length, and β is the weighting parameter. Together Eqs. (2)–(4) form the basis for solving the slip distribution using least-squares inversion. Increasing the weighting of Eq. (3) results in increasing the degree of the conservation constraint. A strict conservation constraint at those intersections results in a block-like deformation model. A very loose conservation constraint results in a fault-patch-only deformation model. The degree of weighting on the conservation constraint is optimally selected from a trade-off curve between the residual chi-squares and the parameter resolution of the model, so that with limited number of model parameters, certain non-block-like deformation features would be allowed, such as permanent or transient strain build-up within the bounding blocks. Our model does not allow uniformly distributed strains within blocks as some block models did (e.g., McCaffrey, 2005), and the residual strains are therefore distributed more around the block boundaries. The locking depths in general are estimated based on the depth distribution of seismicity (Petersen et al., 1996; Shen and Jackson, 2003). Although this was not done in this paper, those depths could also be optimized based on the goodness-of-fitting between model prediction and geodetic observations.

3. GPS data and analysis

Our GPS data for California and its neighboring regions are obtained from two of the Southern California Earthquake Center (SCEC) projects, one is the Working Group on California Earthquake Probabilities (WGCEP) project of California Crustal Motion Map version 1.0 (Shen et al., 2006), and the other is the Southern California Crustal Motion Map version 4.0 (CMM4) (Shen et al., 2011). Although the California Crustal Motion Map version 1.0 includes a draft version of CMM4 in Southern California, the subsequent revision of CMM4 before its final publication has improved the CMM4 data quality significantly. Data were synthesized from multiple sources, including continuous GPS stations from the Southern California Integrated GPS Network (SCIGN) and the Bay Area Regional Deformation network (BARD) for California, the Basin and Range Geodetic Network (BARGEN) for Nevada, and the Pacific Northwest Geodetic Array (PANGA) for southern Oregon. Survey-mode measurements were obtained from hundreds of sites observed by surveyors from government agencies such as US Geological Survey (USGS) and California Department of Transportation (Caltrans), and universities throughout the region. The dataset spans 18 years, from December 1986 to October 2004. The data were processed using the GAMIT/GLOBK software (King and Bock, 2006; Herring, 2002), and daily solutions were combined using the QOCA software (Dong et al., 1998; http://gipsy.jpl.nasa.gov/qoca) to solve for secular velocities and coseismic and postseismic displacements from strong earthquakes that occurred during this time period such as the 1989 Mw 6.9 Loma Prieta, 1992 Mw 6.1 Joshua Tree and Mw 7.3 Landers, 1994 Mw 6.7 Northridge, 1999 Mw 7.1 Hector Mine, and 2003 San Simeon earthquakes. The CMM4 solution included velocities derived from EDM data measured in southern California from 1970 to 1992. Velocity solutions from the two projects are combined together after a rigid body rotation, constrained by velocity solutions from common stations.

Rigorous error analysis was done for the Southern California CMM4 solution, and a statistical test for co-located site velocities showed that the errors are quasi-Guassian (Shen et al., 2011). GPS observation errors are spatially correlated due to shared common errors of satellite orbits. Errors of site velocities derived from GPS data are therefore also correlated spatially, and to a greater degree (up to 70% for adjacent sites) if the data are processed using the double-differencing technique (Shen et al., 2011). Such correlations, however, are greatly reduced in the velocity solution used in this study, since the solution was produced under external constraints, i.e., seven network configuration parameters for rotation, translation, and dilatation of the network of a selected set of sites located in the stable part of the North America plate are tied to the model predicted values of the SNARF 1.0 (Stable North America Reference Frame) model (Shen et al., 2011). Enforcement of these constraints eliminates most of the nominal inter-station correlations in the solution, leaving the velocity uncertainties to reflect mainly the site local errors. This process gives rise to a set of velocities whose individual uncertainties are close to what we expect they should be depending on station type (continuous or campaign mode), duration and frequency of observations ranging from submillimeter/yr to 1–2 mm/yr. As a consequence, they no longer reflect the common errors shared by all neighboring sites. Nevertheless systematic errors resulted from that would be very small in a region spanning only a few hundred kilometers, and should have no significant effect to our current modeling result.

Fig. 1 presents a map view of the combined GPS velocity field with a total of 1403 sites for California and parts of western Nevada and southern Oregon. A sharp decrease in GPS velocity amplitudes is shown across the entire San Andreas Fault system, the eastern California shear zone, and along the Walker Lane near the California and Nevada borders. The GPS velocities are nearly constant across the Sierra Nevada/Great Valley block, suggesting it is a strong rigid block.

To further examine the GPS velocity field along the San Andreas Fault, we plot the GPS velocity profiles along transects perpendicular

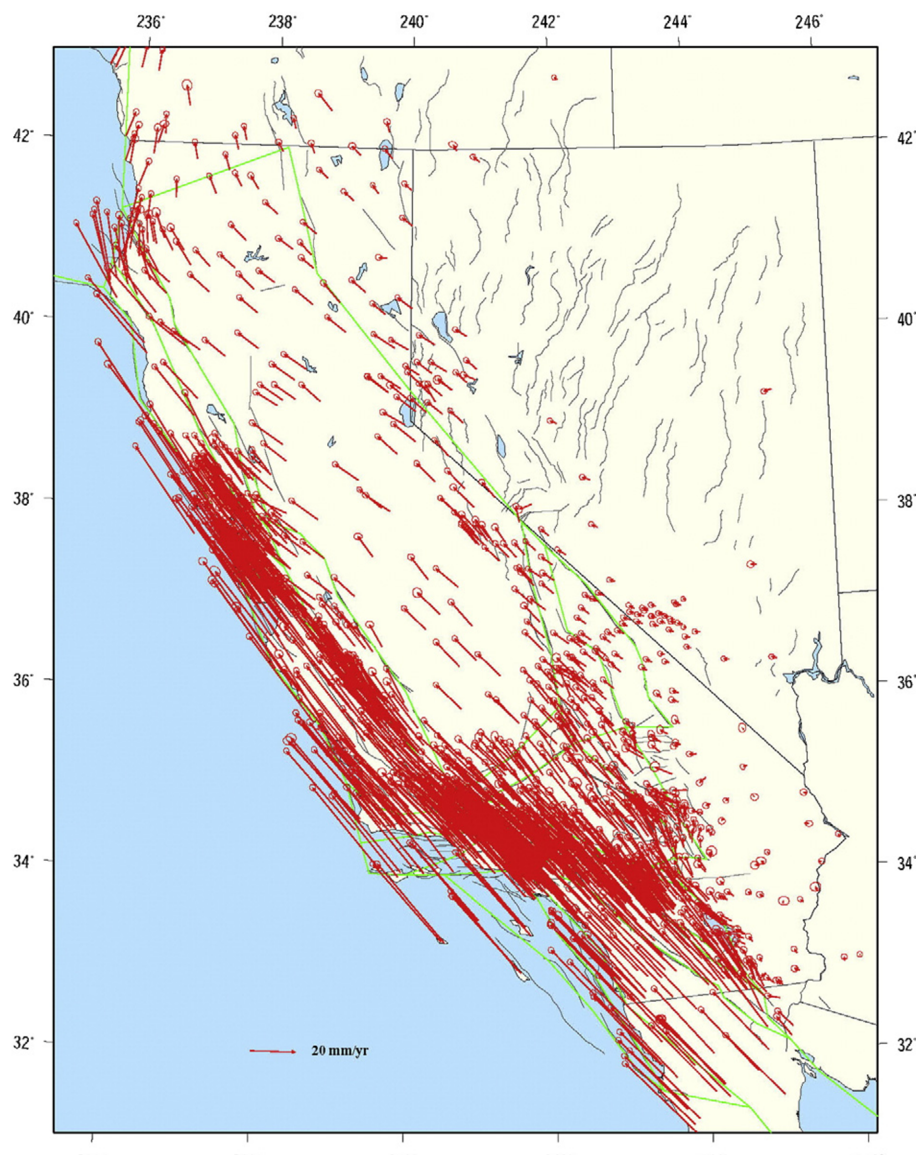

Fig. 1. Distribution of GPS velocity vectors for California and its neighbors, referenced to the North America plate. Error ellipses represent 50% confidence.

to the San Andreas fault zone, i.e., across the Santa Cruz Mountain, central California creeping zone, Cholame, and Carrizo Plain sections (Fig. 2). Red and blue squares are velocity components parallel and perpendicular to the fault respectively.

For the central California creeping segment, since the fault slips all the way to the surface interseismically, the velocity profile across the San Andreas Fault shows an abrupt step-like jump. There are also small but still notable gradients in the fault parallel velocity profile away from the fault, indicating depth dependent creeping rates where the topmost segment releases its energy in periodic creeping episodes (Rolandone et al., 2008).

Instead of a step-like jump in velocity across the creeping section, the Carrizo Plain segment shows a smoothly varying GPS velocity profile that spans about 100 km across the fault zone. This appears to be a classic example of a buried dislocation model with constant slip rates at about 30–35 mm/yr with a locking depth of about 15–20 km deep.

For the Santa Cruz Mountains and Cholame sections, the GPS velocities have gradients steeper than velocities observed in the Carrizo Plain but more gradual than velocities observed in the central California creeping segment. This indicates either a shallower locking depth or a partial locking within the seismogenic zones. Seismicity in the areas shows a locking depth similar to the Carrizo Plain seismic zone (Hauksson, 2000; Hill et al., 1990), suggesting partial locking.

4. California fault network model

Our kinematic fault network model is developed from the SCEC (Field et al., 2009) and USGS (Petersen et al., 2008) fault database for California and nearby states. A relatively complex fault system in the state has led to the complex structure of our fault network model. Shen and Jackson (2003) developed a preliminary version of this model for southern California using a simplified version of the SCEC Community Fault Model (CFM) and Community Block Model (CBM). We start from Shen and Jackson's model, then add the Bay area block model from d'Alessio et al. (2005) for northern California, and further extend it to the entire California and part of its neighboring regions of Oregon and Nevada based on the USGS 2008 Quaternary fault model (Petersen et al., 2008). We revise the Southern California part of the model based on a recent update of the California faults provided in the SCEC UCERF 2 model (Field et al., 2009).

We enclose all fault segments to form blocks in the area. This allows us to compare our results with other block model studies (e.g., McCaffrey, 2005; Meade and Hager, 2005; d'Alessio et al., 2005). Fig. 3 shows a map view of our California fault network model. All the fault network traces are plotted in red and the original SCEC UCERF2 and USGS 2008 Quaternary faults are plotted in black. The model consists of major faults in California and faults off the coast (the Cascadia subduction zone, San Gregorio, Hosgri, Santa Cruz Catalina Ridge, and Palos Verdes faults, etc.) to faults in the continent (the San Andreas, San Jacinto, Elsinore, Hayward, Calaveras, Great Valley, Death Valley, White Wolf, Garlock, Owens Valley, and Newport–Inglewood–Rose Canon faults, etc.). We extended the Cascadia subduction zone 2000 km north and the southern extension of the San Andreas fault 2000 km south to model relative plate motion between the Pacific and the North America Plate and to avoid edge effect at the model boundaries.

The western Transverse Ranges contains numerous smaller faults. Instead of linking those small faults to form many small blocks, we simplify the model by introducing a few larger blocks. Those blocks are bounded by the Anacapa and Santa Cruz Island faults to the south, the Big Pine fault to the north, and the Santa Susana–San Cayetano–Santa Ynez fault in between. The southern part of the region is cut through by the Oak Ridge fault. To the east are the San Gabriel, Sierra Madre, and Cucamonga faults bounding the San Gabriel block at its south and west. For the eastern California shear zone, we divided it into blocks bounded by north–south trending faults of Landers and Gravel Hill-Harper Lake, and by Pisgah-Bullion Mountain all the way to Panamint Valley. This is an over-simplification for a rather intricate tectonic structure, but a lack of sufficient geodetic observations precludes additional complexity. A more detailed fault model in the region (McClusky et al., 2001; Miller et al., 2001) is possible but will sacrifice model resolution significantly.

For the Nevada and northern California bordering area, we simplify the faults into a western Nevada and northern California shear boundary. Separated by the rigid Sierra Nevada and Great Valley Block, the

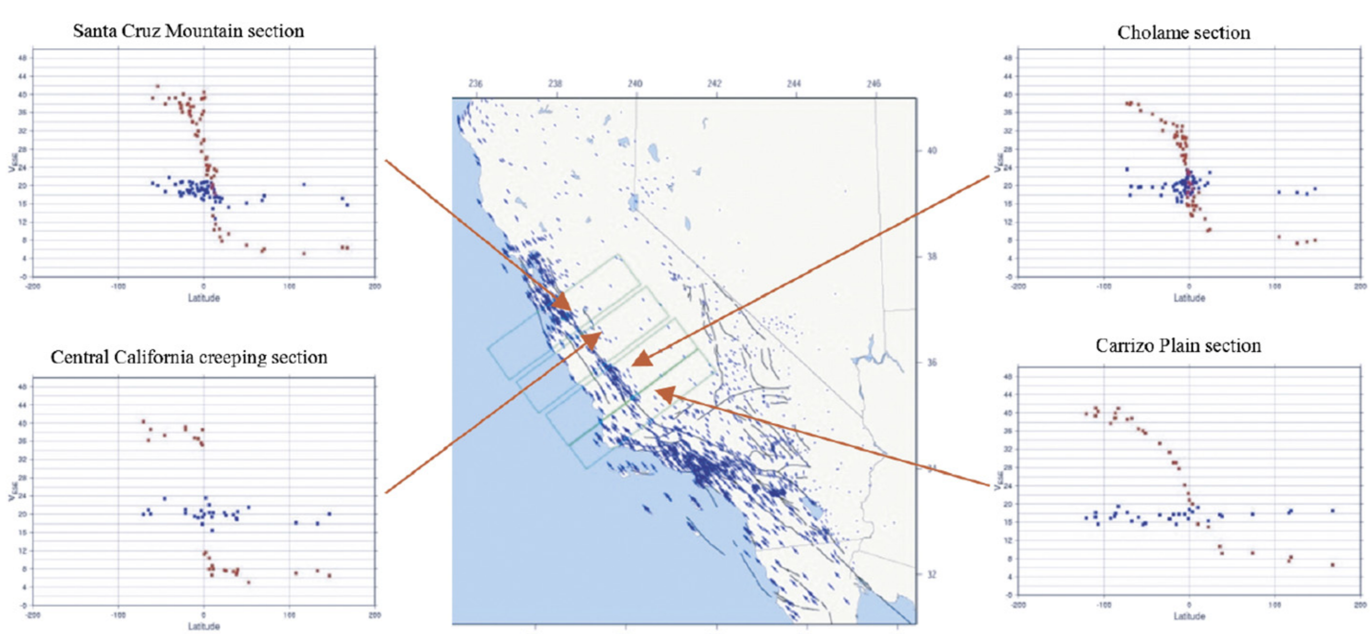

Fig. 2. Profiles of GPS velocities along transects perpendicular to the San Andreas fault from the Santa Cruz Mountains, central California creeping, Cholame, to Carrizo plain segments. Red and blue squares are displacement components parallel and perpendicular to the fault respectively.

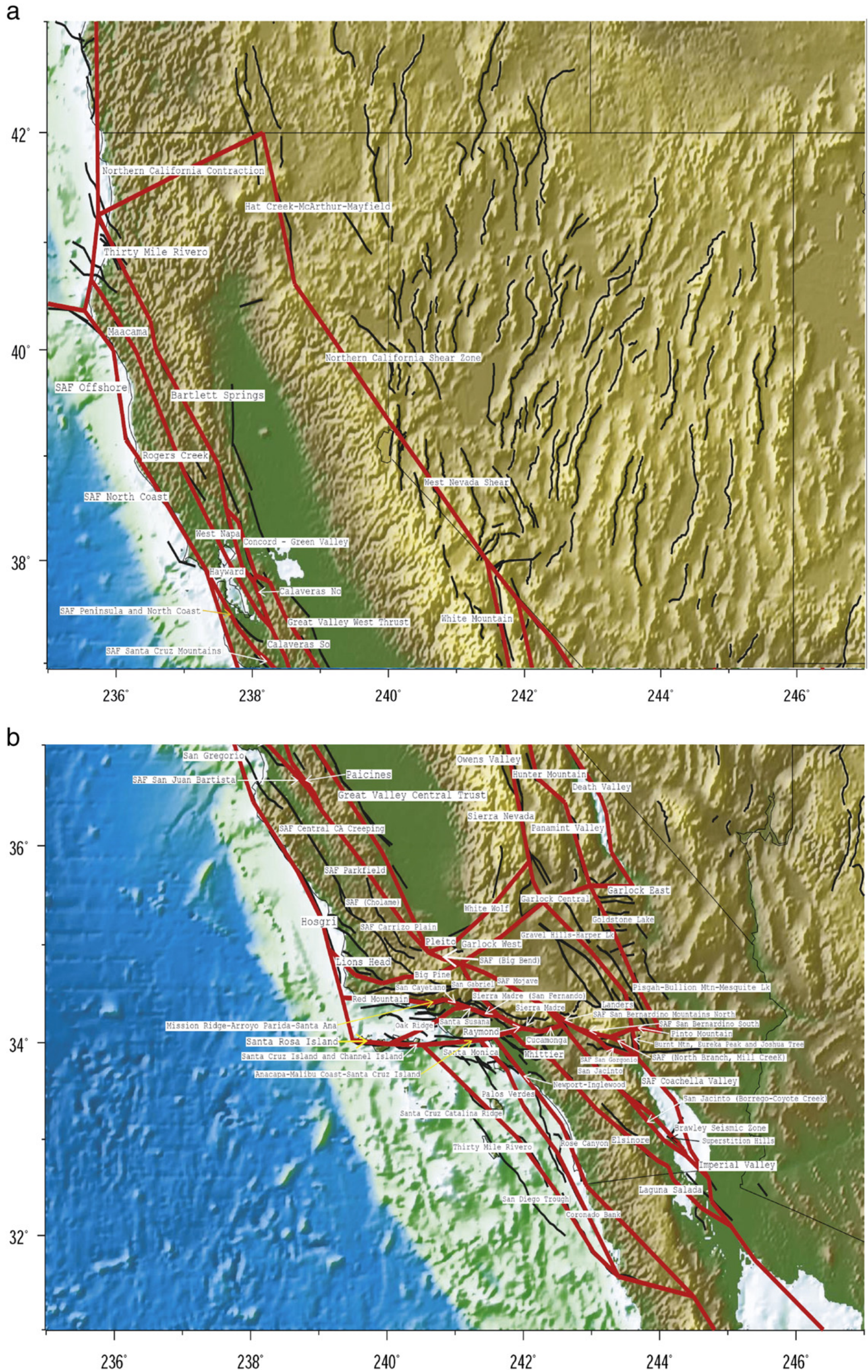

Fig. 3. Map view of the California fault network model (red). Traces in black are faults from the USGS quaternary fault database and UCERF 2 fault database.

Table 1
Fault slip rates along San Andreas based on GPS data inversion with and without geologic data constraints (mm/yr).

Strike slip Rate1	Strike slip Rate2	Spreading Rate1	Spreading Rate2	Locking depth	Fault name
22.9 ± 1.2	22.2 ± 1.8	−1.1 ± 0.8	−4.6 ± 1.5	14.0	Imperial Valley
24.6 ± 1.1	24.0 ± 1.3	7.3 ± 0.9	5.4 ± 1.0	6.0	Brawley Seismic Zone
20.8 ± 1.0	24.3 ± 1.3	0.0 ± 0.7	0.5 ± 1.2	18.0	SAF Coachella Valley
1.8 ± 0.8	6.0 ± 1.9	−1.0 ± 0.5	0.4 ± 0.7	17.7	SAF North Branch, Mill Creek
10.4 ± 1.1	3.5 ± 3.2	−1.3 ± 0.7	1.9 ± 1.4	18.0	SAF San Gorgonio Pass-Garnet Hill
12.6 ± 0.9	3.4 ± 2.6	0.0 ± 0.5	1.1 ± 0.9	18.0	SAF San Bernardino South
13.1 ± 1.0	6.9 ± 1.5	−1.4 ± 0.7	−0.2 ± 1.2	15.0	SAF San Bernardino Mountains North
19.2 ± 0.5	15.4 ± 0.8	−1.7 ± 0.4	−0.8 ± 0.7	14.0	SAF Mojave
26.5 ± 0.7	23.5 ± 1.3	−2.0 ± 0.5	−4.5 ± 0.9	18.0	SAF Big Bend
28.7 ± 0.7	22.9 ± 1.0	0.1 ± 0.5	−1.8 ± 0.9	15.0	SAF Carrizo Plain
30.0 ± 0.7	27.5 ± 1.0	−1.5 ± 0.4	−1.6 ± 0.7	15.0	SAF Cholame
30.1 ± 0.5	27.6 ± 0.8	−1.6 ± 0.3	−1.9 ± 0.5	15.0	SAF Parkfield
31.7 ± 0.8	30.4 ± 1.0	−1.5 ± 0.6	−3.5 ± 0.9	5.0	SAF Central CA Creeping
25.3 ± 0.7	21.5 ± 0.9	−0.5 ± 0.5	−1.0 ± 0.7	0.0	SAF San Juan Bartista
19.9 ± 0.6	22.5 ± 0.9	−0.0 ± 0.4	0.1 ± 0.7	15.0	SAF Santa Cruz Mountains
17.3 ± 1.1	19.9 ± 1.7	1.3 ± 0.8	4.7 ± 1.6	15.0	SAF Peninsula and North Coast
23.0 ± 0.9	24.3 ± 1.4	0.0 ± 0.6	2.4 ± 1.2	15.0	SAF North Coast
22.7 ± 0.8	22.3 ± 1.3	3.8 ± 0.6	13.4 ± 1.2	15.0	SAF Offshore

For strike slip rate, right-lateral is positive.
For spreading rate, extensional spreading is positive.
Rate1 is the preferred slip rates from GPS data inversion with geologic constraints.
Rate2 is for GPS data inversion without geologic constraints.

effect of this simplified boundary on the slip rates over other California faults should be negligible. We choose to have this boundary cutting through the east side of the northern Walker Lane fault zone because of a much greater GPS velocity gradient across the east side than across the west side of the northern Walker Lane fault zone. The northern boundary of the block containing the Sierra Nevada and Great Valley is selected according to the observed shortening localized along the section (Hammond and Thatcher, 2004).

We have introduced shallow creep in some of the fault segments, for example, along the central California Creeping segment, Calaveras, Paicines, Hayward, Imperial Valley, Brawley seismic zone. We also allow partial locking for the northern Parkfield and southern Santa Cruz Mountain segments of the San Andreas. The creeping occurs at a constant rate from the surface to 10 km depth for most creeping faults except the central California creeping zone and the Brawley seismic zone. In the central California creeping zone, we assume depth dependent creep rates from the surface to 5 km depth and from 5 km to 10 km depth, respectively. The creeping depth along the Brawley seismic zone is set to be equal to its locking depth because of its shallow seismogenic layer (Table 1). The amount of creep along those creeping segments is determined from inversion of the GPS observations.

The fault locking depths listed in Tables 1–9 are determined based on seismicity depth distribution along faults available in the literature (e.g. Hauksson, 2000; Hill et al., 1990). We assume that all fault segments are vertical and use spreading and shortening across fault segments as proxy for dip slip faulting. Instead of inverting for Euler pole rotation parameters for each block, we invert for the fault slip rate parameters directly from surface geodetic observations.

Table 2
Fault slip rates along Hayward to Maacama (mm/yr).

Strike slip Rate1	Strike slip Rate2	Spreading Rate1	Spreading Rate2	Locking depth	Fault name
9.2 ± 0.8	5.9 ± 1.1	0.1 ± 0.5	−0.9 ± 0.9	12.0	Hayward
11.3 ± 1.3	9.8 ± 1.9	0.0 ± 0.8	−0.9 ± 1.7	12.0	Rogers Creek
12.9 ± 0.9	14.8 ± 1.3	0.0 ± 0.6	−2.7 ± 1.2	12.0	Maacama

5. Results

Before we compute our final inverse solutions, we optimize the gross weighting parameter α in Eq. (3) for the continuity constraints on slip rate vectors across fault node points. This gross weighting parameter trades off with both the model resolution defined by the diagonal elements of the model resolution matrix (Menke, 1989) and data variance reduction. When it approaches to infinity, a strict continuity condition is imposed on slip-rate-vectors across any nodal points. This leads to a strict block-like behavior of the model. A question arises on whether other models of lesser constraints perform significantly better than this model. To answer the question, we first compute the F-test ratio of this strict block-like model to other models with a range of different weights. The higher the ratio, the more significant the difference of reduced data variances between the strict block-like model and other testing models. Fig. 4a shows these ratios versus weighting parameter α. The red line marks the threshold above which the reduced data variances of other testing models are significantly smaller than that of the strict block-like model at a 95% confidence level. As an end member, the strict block-like model has the least free model parameters measured by the total number of model resolution. As the other end member, the completely segmented fault-based model with zero continuity constraints best fit the GPS observations. The strict block-like model with the least slip rate variability along block boundaries has not only

Table 3
Fault slip rates along Calaveras to Bartlett Springs (mm/yr).

Strike slip Rate1	Strike slip Rate2	Spreading Rate1	Spreading Rate2	Locking depth	Fault name
10.0 ± 0.9	12.1 ± 1.1	−2.2 ± 0.8	−3.7 ± 0.9	11.0	Paicines
14.9 ± 0.7	15.9 ± 1.0	−0.5 ± 0.5	−3.4 ± 0.8	11.0	Calaveras So
6.9 ± 1.0	10.7 ± 1.7	−1.3 ± 0.7	−3.1 ± 1.5	13.0	Calaveras No
7.2 ± 1.1	4.5 ± 2.2	−0.2 ± 0.7	−1.2 ± 1.4	14.7	Concord-Green Valley
2.7 ± 0.8	7.7 ± 2.3	0.0 ± 0.7	0.0 ± 1.5	10.0	West Napa
9.5 ± 1.0	10.1 ± 1.1	−1.1 ± 0.7	−2.9 ± 1.1	15.0	Bartlett Springs
7.2 ± 1.7	5.6 ± 1.8	−9.9 ± 1.5	−9.1 ± 1.6	15.0	Trinidad-McKinleyville

Table 4
Fault slip rates along Transverse Ranges (mm/yr).

Strike slip Rate1	Strike slip Rate2	Spreading Rate1	Spreading Rate2	Locking depth	Fault name
−0.2 ± 0.7	1.4 ± 1.3	0.8 ± 0.6	1.4 ± 1.2	15.6	Raymond
−0.9 ± 0.5	3.5 ± 1.1	−0.6 ± 0.5	−1.6 ± 0.9	17.3	Santa Monica
−2.1 ± 0.7	−1.7 ± 1.4	−3.6 ± 0.7	−8.2 ± 1.3	15.5	Anacapa–Malibu Coast–Santa Cruz Island
−1.5 ± 0.9	−0.7 ± 2.0	−1.7 ± 0.8	−5.5 ± 1.6	13.3	Santa Cruz Island and Channel Island
−2.3 ± 0.8	−3.1 ± 1.6	−1.1 ± 0.8	−2.7 ± 1.3	8.7	Santa Rosa Island
−0.8 ± 0.5	−2.1 ± 1.1	−1.3 ± 0.5	0.1 ± 0.8	19.4	Oak Ridge
−0.8 ± 0.6	−1.8 ± 1.4	−2.6 ± 0.6	−2.1 ± 1.1	13.0	Sierra Madre (San Fernando)
−0.3 ± 0.6	−1.3 ± 1.3	−4.2 ± 0.7	−3.0 ± 1.1	16.3	Santa Susana
−0.5 ± 0.7	0.1 ± 1.5	−3.5 ± 0.8	−2.5 ± 1.2	16.0	San Cayetano
−0.7 ± 0.4	−1.4 ± 0.7	−1.2 ± 0.3	−1.7 ± 0.6	7.6	Mission Ridge-Arroyo Parida-Santa Ana
−0.3 ± 0.7	−0.7 ± 1.4	−0.3 ± 0.7	0.3 ± 1.3	14.1	Red Mountain
−1.1 ± 0.6	−1.7 ± 1.1	−3.2 ± 0.7	−4.0 ± 1.0	7.8	Cucamonga
−0.9 ± 0.5	−0.2 ± 0.9	−3.0 ± 0.4	−3.5 ± 0.8	14.2	Sierra Madre
1.1 ± 0.5	3.5 ± 1.1	−1.7 ± 0.5	−1.1 ± 0.8	14.7	San Gabriel
3.1 ± 0.9	3.8 ± 1.0	−2.2 ± 0.7	−1.3 ± 1.0	14.1	Whittier

the worst fit to the GPS data but also essentially zero interseismic off-fault strain accumulation. The purely segmented fault-based model with the most slip rate variability along block boundaries produces not only the best fit to the GPS data but also the most interseismic off-fault strain accumulation among all possible models that fit to the GPS and geologic observations. With an appropriate trade-off between the two end member models, it is clear that the optimal model could be found. Fig. 4b shows the total number of model resolutions versus the reduced χ^2 from inversions with a series of different weighting parameter α. We have excluded models that do not fit the GPS observations significantly better than the strict block-like model. An optimal weighting was picked at 128.0 (red dot) with an optimal trade-off between the model resolution and data variance reduction for inversions using GPS data only. Since the fault system in the region is dominated by strike slip faults, we also introduce an additional minimization on slip rates along the fault normal direction based on Eq (4). Fig. 5 shows a trade-off between the reduced χ^2 and l_2-norm of the fault normal slip rates with different weighting constraints. Comparing the ranges in the reduced χ^2 between Figs. 5 and 4, the influence of this weighting constraint on the overall fit is much weaker than that of the continuity constraint. An optimal weighting β of 32.0 (red dot) corresponding to 5500 mm^2/yr^2 in the sum of shortening/extension slip rate squares was picked based on an optimal trade-off of the least reduced χ^2 and the fault normal slip rates. With those weighting parameters, we find a total number of resolutions of 130.2 out of a total number of model parameters of 380 and a reduced χ^2 of 1.75 for the final inversion using GPS data only. The significant reduction in model resolution indicates strong smoothing or model regulation on slip rates between connecting fault segments.

Fig. 6 shows a model resolution distribution across the fault network for the strike slip rates without the continuity constraints. Except near the Parkfield and San Bernardino fault segments, the model resolution varies between 80 and 100% with an average of 96%, suggesting a near perfect data coverage in the study area. Fig. 7a shows the same model resolution distribution but with the optimally weighted continuity constraints. The model resolution is higher for longer fault segment and for faults located near densely distributed GPS stations. Overall the model resolution spans from 0 to 100%, but the average is low at 22.8%. Any incompleteness in the data coverage accounts for a fraction of 4% loss, due partly to the lack of data in the far field to effectively constrain the segments at the edges and in Parkfield and San Bernardino to discriminate fine scale fault structures. The rest of 73.2% reduction is caused by the continuity constraints. Fig. 7b shows the same model resolution but normalized by their corresponding fault segment length. The normalized model resolution appears to be distributed more evenly in space, suggesting a reasonable uniform sampling of the data space by the model. For the fault normal component without the continuity constraints, the average model resolution is 41.4%, due mostly to an additional minimization constraint on the fault normal component of the slip rates. However, the final resolution distribution for the optimally weighted inversion using GPS data only is nearly identical to that of the fault parallel component with an average of 21.8%. The continuity constraints, in this case, account for a merely 19.6% losses in the resolution.

Table 5
Fault slip rates along Eastern California Shear Zone and Southern Walker Lane (mm/yr).

Strike slip Rate1	Strike slip Rate2	Spreading Rate1	Spreading Rate2	Locking depth	Fault name
5.6 ± 0.8	17.6 ± 2.1	0.7 ± 0.8	3.1 ± 2.0	15.0	Burnt Mtn, Eureka Peak and Joshua Tree
6.6 ± 0.6	14.1 ± 1.1	−0.1 ± 0.5	1.0 ± 1.0	15.1	Landers
3.4 ± 0.7	1.6 ± 1.1	−0.7 ± 0.6	−1.0 ± 0.9	11.4	Gravel Hills-Harper Lk
0.1 ± 0.6	1.3 ± 1.1	1.6 ± 0.5	1.3 ± 0.9	13.6	Sierra Nevada
3.3 ± 0.8	4.7 ± 1.6	2.7 ± 0.8	4.5 ± 1.5	13.5	Owens Valley
3.5 ± 0.9	7.4 ± 1.7	1.0 ± 0.8	3.5 ± 1.6	13.0	White Mountain
−5.3 ± 0.6	−1.6 ± 1.2	1.5 ± 0.4	3.3 ± 1.0	15.5	Pinto Mountain
7.4 ± 0.5	10.8 ± 1.0	0.8 ± 0.5	−0.8 ± 0.9	13.1	Pisgah-Bullion Mtn-Mesquite Lk
13.2 ± 1.4	8.0 ± 1.6	0.0 ± 1.2	0.1 ± 1.4	12.4	Goldstone Lake
6.0 ± 0.9	4.9 ± 1.2	2.5 ± 0.6	4.0 ± 1.2	13.0	Panamint Valley
5.1 ± 0.9	2.9 ± 1.2	1.3 ± 0.8	0.1 ± 1.3	12.4	Hunter Mountain
3.4 ± 0.5	2.5 ± 0.6	0.1 ± 0.3	−0.5 ± 0.6	13.0	Death Valley

Table 6
Fault slip rates along Garlock and adjacent faults (mm/yr).

Strike slip Rate1	Strike slip Rate2	Spreading Rate1	Spreading Rate2	Locking depth	Fault name
−2.6 ± 0.8	−5.7 ± 1.9	−2.2 ± 0.7	−3.4 ± 1.4	13.6	Pleito
−2.4 ± 0.7	−3.0 ± 1.1	−2.9 ± 0.7	−0.4 ± 1.0	14.6	White Wolf
−0.4 ± 0.6	1.3 ± 1.0	0.6 ± 0.5	1.4 ± 0.8	10.0	Lions Head
−5.1 ± 0.8	−2.7 ± 1.0	−1.1 ± 0.7	−1.7 ± 0.8	11.0	Big Pine
−2.0 ± 1.0	−1.9 ± 1.1	−1.8 ± 0.6	−4.2 ± 1.0	14.7	Garlock West
−5.4 ± 0.9	−4.8 ± 1.4	−4.3 ± 0.6	−4.8 ± 1.0	11.5	Garlock Central
−2.7 ± 1.2	−1.3 ± 1.8	−1.0 ± 0.8	−2.5 ± 1.5	11.5	Garlock East

Fig. 8a shows the residual velocity vectors for inversion using GPS data only. Those residual vectors are given by the differences between the observed and model predicted GPS velocities with a mean residual vector length of 1.5 mm/yr. The relatively large misfits in the Landers/Hector Mines area could be partly due to inaccurate modeling of the long term postseismic deformation during the data processing. Overall we do not observe any systematic trend in the residuals that might suggest model bias. The model accounts for all the major features observed in the GPS velocity field shown in Fig. 3. Fig. 8b shows the residual velocities for inversion with the geologic slip rate constraints. The mean residual vector length in this case is 1.6 mm/yr despite no obvious visual difference in comparison with the residual results of inversion using GPS data only shown in Fig. 8a. The total number of model resolution is 108 and the reduced χ^2 is 2.2. In this joint inversion, geologic constraints are introduced by equating the slip rates at any given segments to that of the geologic estimates where they are available. Since error information is not available in the UCERF 2 model, we assume that the standard errors for the geologic rates are 1.0 mm/yr for any geologic rates below 2 mm/yr and 2.0 mm/yr for rates above 2 mm/yr. The additional model resolution reduction of the joint inversion is because geologic data are used as constraints rather than input data like the GPS observations.

Our preferred model is the inversion with geologic slip rate constraints. However the inversion based on the GPS data only provides us insight into how additional geologic constraints improve the inversion. Fig. 9a and b shows the strike slip rate components over the fault network for inversions without and with the geologic constraints, respectively. About 70% of the relative motion between the Pacific Plate and the North American Plate has been accommodated by the San Andreas, San Jacinto, Hayward, Calaveras, and Hayward fault system. Another 20% of the relative plate motion is accommodated by the eastern California shear zone and the Walker Lane fault system.

A total sum of 39 mm/yr is found for the relative motion accommodated by the Bay area faults. The total rates increases to 45 mm/yr further north across the northern coast segment of the San Andreas, Maacama, and Bartlett Springs faults. Slip rates vary from 19.9 ± 0.6 mm/yr along the Santa Cruz Mountains segment to the north based on inversion with geologic constraints (Table 1), from 9.2 to 12.9 mm/yr along the Hayward to Maacama (Table 2), and from 14.9 to 2.7 mm/yr along the central Calaveras to West Napa (Table 3). For the West Napa and Green Valley fault segments, the sum of slip rates of the two amounts to 8–12 mm/yr rate, consistent with the result of d'Alessio et al. (2005). Individual slip rates are 2.7 ± 0.8 mm/yr and 7.2 ± 1.1 mm/yr for the West Napa and Green Valley faults, respectively, consistent with the UCERF 2 model. These results, however, differ significantly from that out of the GPS only inversion, which shows slip rates of 7.7 ± 2.3 mm/yr and 4.5 ± 2.2 mm/yr for the west Napa and Green Valley faults, respectively. The combined inversion rates along the Hayward and Calaveras faults are consistent with the local UCERF2 geologic results of 9 and 15 mm/yr, respectively. However, the GPS only rate along Hayward is significantly slower than that of the geologic rate.

Table 1 also listed the preferred slip rate along the central California creeping zone at about 31.7 ± 0.8 mm/yr. The rate is about 28.7–30.1 along the Carrizo Plain and Parkfield segments. These rates in the central San Andreas system are smaller compared to other geodetic studies (e.g., Meade and Hager, 2005) and geologic studies (e.g., Sieh and Jahns, 1984; Sims, 1994). Slip rates along the Mojave segment of the San Andreas is rather low at 15.4 ± 0.8 mm/yr for the inversion without the geologic constraints, in comparison with that of the geologic preferred rates of 35 mm/yr (Weldon et al., 2002, 2008). With the geologic constraints, the inversion rate increases to 19.2 ± 0.5 mm/yr, still well below the geologic estimates but around their low bound of 20 mm/yr (Weldon et al., 2002). For the San Bernadino Mountains North segment, our slip rate estimate is 6.9 ± 1.5 mm/yr using GPS data only. Meade and Hager (2005) reported a slip rate along this segment at about 5.1 mm/yr. Both slip rate estimates are significantly below the range of the geologic values of 11–24 mm/yr (McGill et al., 2010; Weldon and Sieh, 1985). With the geologic constraints, our estimate increases to 13.1 ± 1.0 mm/yr, getting to the range of the geologic estimates. This suggests that the solution is not very well resolved based on GPS data only for the San Bernardino fault segment. Using the GPS data

Table 7
Fault slip rates along off-coast faults of California (mm/yr).

Strike slip Rate1	Strike slip Rate2	Spreading Rate1	Spreading Rate2	Locking depth	Fault name
2.6 ± 1.5	5.2 ± 1.9	−3.3 ± 1.1	−2.2 ± 1.5	8.3	San Diego Trough
4.2 ± 1.9	5.4 ± 2.4	−1.3 ± 1.5	−0.9 ± 2.0	9.6	Thirty Mile Rivero
2.4 ± 1.0	2.0 ± 1.3	−3.4 ± 0.7	1.2 ± 1.0	11.0	Santa Cruz Catalina Ridge
2.0 ± 1.1	−1.0 ± 1.7	−0.2 ± 0.7	−2.6 ± 1.6	8.6	Coronado Bank
3.9 ± 0.8	1.9 ± 1.3	−1.9 ± 0.5	−6.0 ± 1.2	13.6	Palos Verdes
0.6 ± 0.8	0.5 ± 1.7	−0.3 ± 0.8	−1.7 ± 1.6	7.7	Rose Canyon
3.0 ± 0.7	4.1 ± 1.4	−2.0 ± 0.6	−1.1 ± 1.6	12.6	Newport-Inglewood
−0.4 ± 0.6	−1.8 ± 0.9	−0.3 ± 0.4	2.2 ± 0.7	7.5	Hosgri
3.9 ± 0.9	3.8 ± 1.3	−1.5 ± 0.7	−1.5 ± 1.3	12.0	San Gregorio

Table 8
Fault slip rates along San Jacinto and other adjacent faults (mm/yr).

Strike slip	Strike slip	Spreading	Spreading	Locking depth	Fault name
Rate1	Rate2	Rate1	Rate2		
7.3 ± 0.7	15.5 ± 1.9	−0.9 ± 0.4	−1.8 ± 0.9	15.9	San Jacinto (Borrego-Coyote Creek)
10.7 ± 0.9	5.0 ± 2.9	−1.8 ± 0.5	−1.9 ± 1.2	12.6	Superstition Hills
10.7 ± 0.5	11.2 ± 0.9	0.1 ± 0.3	−0.6 ± 0.7	16.8	San Jacinto
2.6 ± 0.7	0.6 ± 0.8	1.2 ± 0.5	4.0 ± 0.7	13.3	Laguna Salada
3.4 ± 0.6	2.5 ± 0.9	1.0 ± 0.5	1.5 ± 0.8	16.0	Elsinore

only, the slip rate along the San Gorgonio Pass segment of the San Andreas is significantly smaller than that along the Mill Creek fault branch. Given the separation distance between the two branches and few data available to constrain the subtle difference on surface deformation caused by buried slip along those two closely spaced fault segments, additional data will be critical to provide more reliable estimates. Consequently the results benefited from the geologic constraints provide consistent rates with the UCERF 2 geologic estimates. Along the Coachella Valley segment of the San Andreas, Imperial Valley, and San Jacinto fault (see Table 1 and Table 8), our results are consistent with the UCERF 2 model based on geologic estimates or consensus.

Fig. 10a and b shows the normal components of the slip rates over the fault network determined from inversions without and with the geologic constraints, respectively. Within the Transverse Ranges, there are series of thrust faults: the Cucamonga, Raymond, and Santa Monica faults in the south, the Oak Ridge, Santa Susana, San Cayetano, Mission Ridge, and Big Pine faults in the north, bounded by the Sierra Madre and San Gabriel faults to the east. Slip rates amount those faults are listed in Table 4. These faults accommodate 0.3–4.2 mm/yr of shortening motion. Shortening rates from inversions with geologic constraints amount to less than half of that without the constraints. Also the shortening along the Big Pine, Cucamonga, Santa Susana, San Cayetano, and Mission Ridge faults decreases from east to west, in agreement with the counterclockwise rotation in the area. Significant shortening is also found across the Whittier thrust fault.

In the eastern California Shear Zone, strike slip rates are 14.1 ± 1.1, 4.7 ± 1.6, and 7.4 ± 1.7 mm/yr from the Landers through Owens Valley to White Mountain faults, respectively, for inversion using GPS data only, and are around 6.6 ± 0.6, 3.3 ± 0.8 and 3.5 ± 0.5 mm/yr, respectively, for inversion with the geologic constraints (Table 5). The preferred geologic rate is 2.8 mm/yr and a maximum rate of 4.5 mm/yr for the Owens Valley fault (Kirby et al., 2008). Strike slip rates are 10.8 ± 1.0, 8.0 ± 1.6, 4.9 ± 1.2, and 2.9 ± 1.2 mm/yr from the Pisgah, Goldstone, Panamint Valley, to Hunter Mountain faults, respectively, for inversion using GPS data only, and are 7.4 ± 0.5, 13.2 ± 1.4, 6.0 ± 0.9, and 5.1 ± 0.9 mm/yr for inversion with the geologic constraints (Table 5), respectively. These slip rate estimates along the Owens Valley, White Mountain, and Goldstones faults are similar to the preferred results of Meade and Hager (2005). Our high slip rates for the Landers and Pisgah faults might be in part affected by the Landers and Hector Mine postseismic deformation. But the persistent high slip rates further north along the Owens Valley fault and the Goldstones and Panamint Valley faults could only point to a higher present-day tectonic stressing rate compared to the geological average over times (Gourmelen et al., 2011). Another possibility could be that due to the high spatial density of faults, significant off fault deformation and

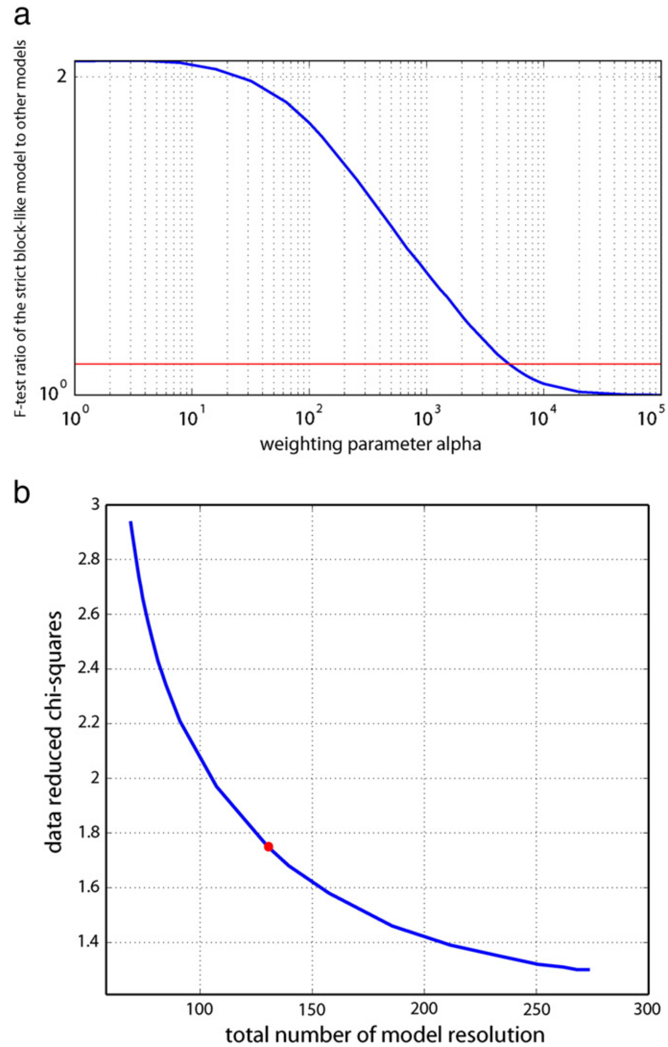

Fig. 4. (a) Degree of fault slip continuity assessment using F-test. The strict block-like model has a gross weighting parameter α approaching infinity. The red line marks the threshold above which variances of other models are smaller than that of the strict block-like model significantly at a 95% confidence level. (b) Plot of the total number of resolution versus the reduced chi-squares for different weighting parameters.

Table 9
Fault slip rates along other northern California faults or shear/contraction zones (mm/yr).

Strike slip	Strike slip	Spreading	Spreading	Locking depth	Fault name
Rate1	Rate2	Rate1	Rate2		
0.9 ± 0.6	0.3 ± 1.0	−0.7 ± 0.5	0.2 ± 0.7	11.4	Great Valley Central Trust
0.8 ± 0.8	0.5 ± 1.4	−1.4 ± 0.7	−1.0 ± 1.2	9.6	Great Valley West Thrust
−0.9 ± 1.1	0.7 ± 1.2	−3.8 ± 0.8	−4.2 ± 0.8	15.0	Northern California Contraction
5.7 ± 0.9	6.0 ± 0.9	−1.4 ± 0.7	−0.7 ± 0.8	13.0	West Nevada Shear
1.8 ± 1.0	2.3 ± 1.1	−1.1 ± 0.8	−0.6 ± 0.9	13.0	Northern California Shear Zone
1.0 ± 0.8	1.4 ± 1.3	1.7 ± 0.6	2.9 ± 0.8	9.6	Hat Creek-McArthur-Mayfield

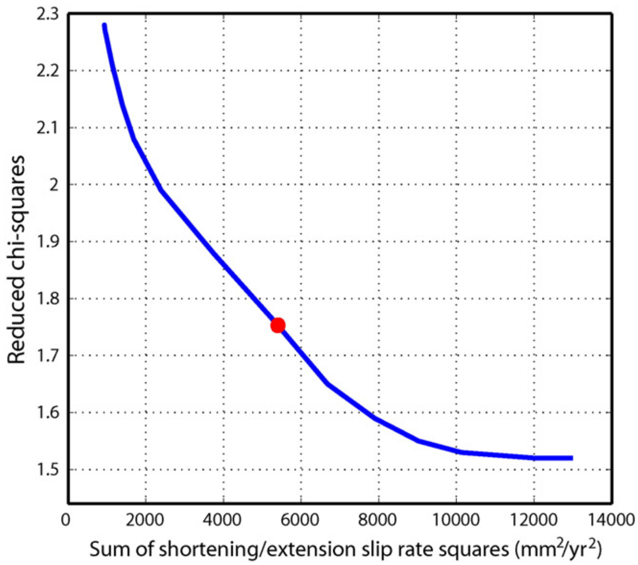

Fig. 5. Plot of the sum of normal slip rate squares versus the reduced chi-squares for different weighting parameters. The red dot shows the optimal trade-off between the two.

slips along adjacent branching faults may not be captured by the geologic study, resulting in lower geologic estimates (Oskin et al., 2007). For the Pinto Mountain fault near the southern end of this shear zone, our estimates show an average of 5.3 ± 0.6 and 1.6 ± 1.2 mm/yr left-lateral slip rates for inversions with and without geologic constraints, respectively. The shortening and extension rates in this area are in qualitative agreement with that of the UCERF 2 model.

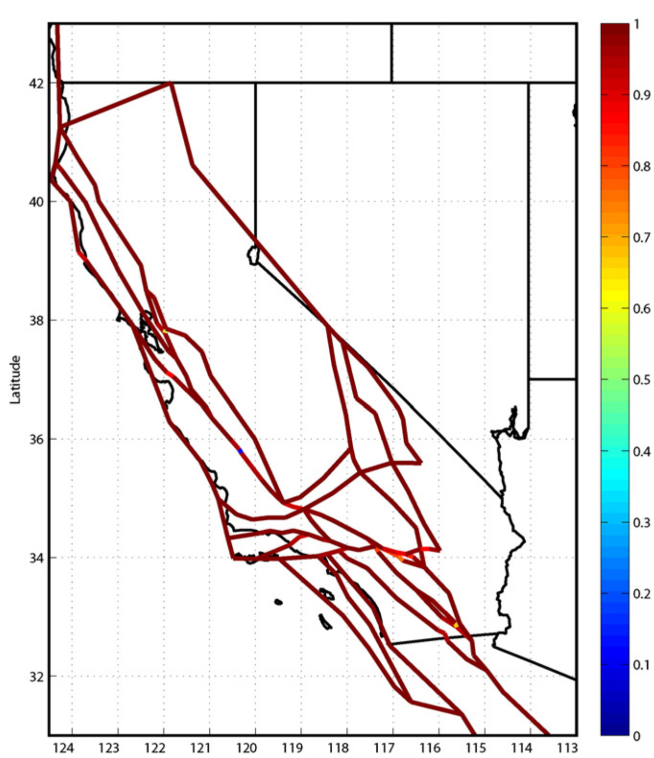

Fig. 6. Map view of the model resolution distribution across the fault network for the fault parallel component of slip rate vectors for an inversion without any continuity constraints or a completely segmented fault-based model.

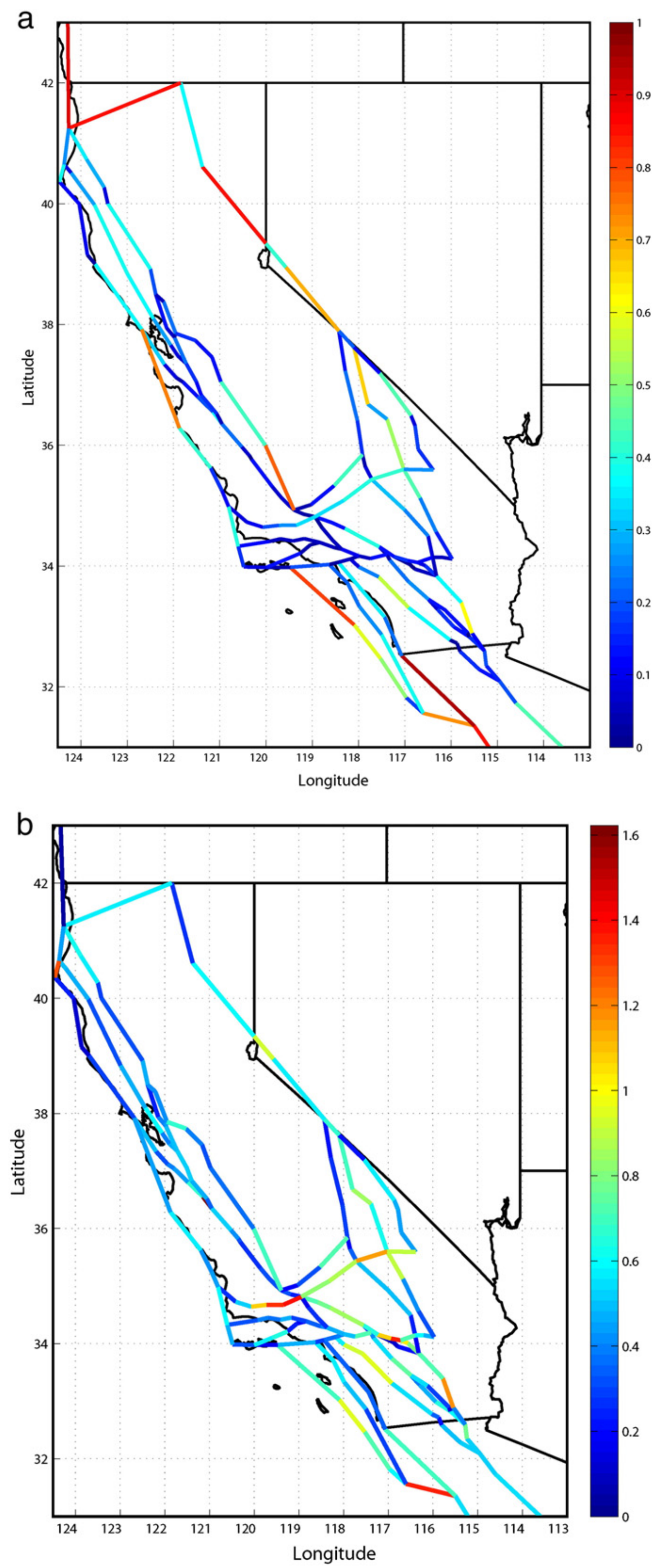

Fig. 7. (a) Model resolution distribution for strike slip-rates across the fault network. (b) Map view of the same model resolution in (a) but normalized by each fault segment length. Colors are in 1/degree.

For the Garlock fault, our estimates show rates of 1.9 ± 1.1, 4.8 ± 1.4 and 1.3 ± 1.8 mm/yr for the west, central and east segments of the fault, respectively, for inversion using GPS data only (Table 6). Our inversion result using GPS data only significantly underestimates the observed rates of 7.0 mm/yr in the central Garlock fault by McGill and Sieh (1993) and of 3.0 mm/yr in the east Garlock from Field et al. (2009). Other block-model based GPS data inversion studies show similar significant discrepancy with the geologic estimates along Garlock (e.g., Meade and Hager, 2005). However, our preferred lesser block-like results with geologic constraints for the west, central and east Garlock segments are 2.0 ± 1.0, 5.4 ± 0.9, and 2.7 ± 1.2 mm/yr, respectively, in close agreement with the geologic rates of 1.6–3.3, 7.0 and 3.0 mm/yr (Field et al., 2009; LaViolette et al., 1980; McGill and Sieh, 1993), respectively. The two end member models obtained in our previous F-test exercise show rates of 1.2 ± 0.4, 0.5 ± 0.4, and 1.0 ± 0.5 mm/yr for the west, central and east Garlock segments, respectively, for the purely block-like elastic model, and 3.7 ± 1.5, 7.3 ± 1.4, and 1.8 ± 1.5 mm/yr, respectively, for the purely segmented fault based model. Our F-test result suggests all less block-like models (including the end member segmented fault based model) fit the data significantly better at a 95% confidence level than the purely block-like elastic model. Johnson et al. (2007) have introduced a viscoelastic response model to provide an alternative explanation to the observed Garlock slip rates. All these results suggest that either there are significant transient slip motions along the Garlock fault or the blocks separated by the Garlock fault may not act exactly block-like.

Table 7 lists slip rates along the off-coast faults in California. For the off-coast faults in southern California, there are only a few GPS stations to provide constraints on the slip rate estimates. We have simplified the off-coast faults in this region to only two fault systems, the Coronado Bank and Palos Verdes fault system, and the Santa Cruz-Catalina Ridge and San Diego Trough fault system. The preferred strike slip rates along the Coronado Bank and Palos Verdes fault system range from 2.0 ± 1.1 to 3.9 ± 0.8 mm/yr in comparison with the 3.0 mm/yr from the UCERF 2 model. Strike slip rates along the Santa Cruz-Catalina Ridge and San Diego Trough fault system range from 2.4 to 4.2 mm/yr. For the Hosgri fault along the central coast region, slip rates range from near 0.4 ± 0.6 to 1.8 ± 0.9 mm/yr left lateral for inversion with and without geologic constraints, respectively. Due to the lack of geologic slip rate measurements, slip rates along the off-shore fault system are not well constrained given GPS data alone. Strike slip rate along the northern coast fault of San Gregorio is around 3.8–3.9 mm/yr for both inversions, which is within the geologic rate of 3–9 mm/yr (Weber, 1994) but significantly below the preferred UCERF2 rate of 5.7 m/yr. Slip rates for other northern California faults/zones are listed in Tables 8–9.

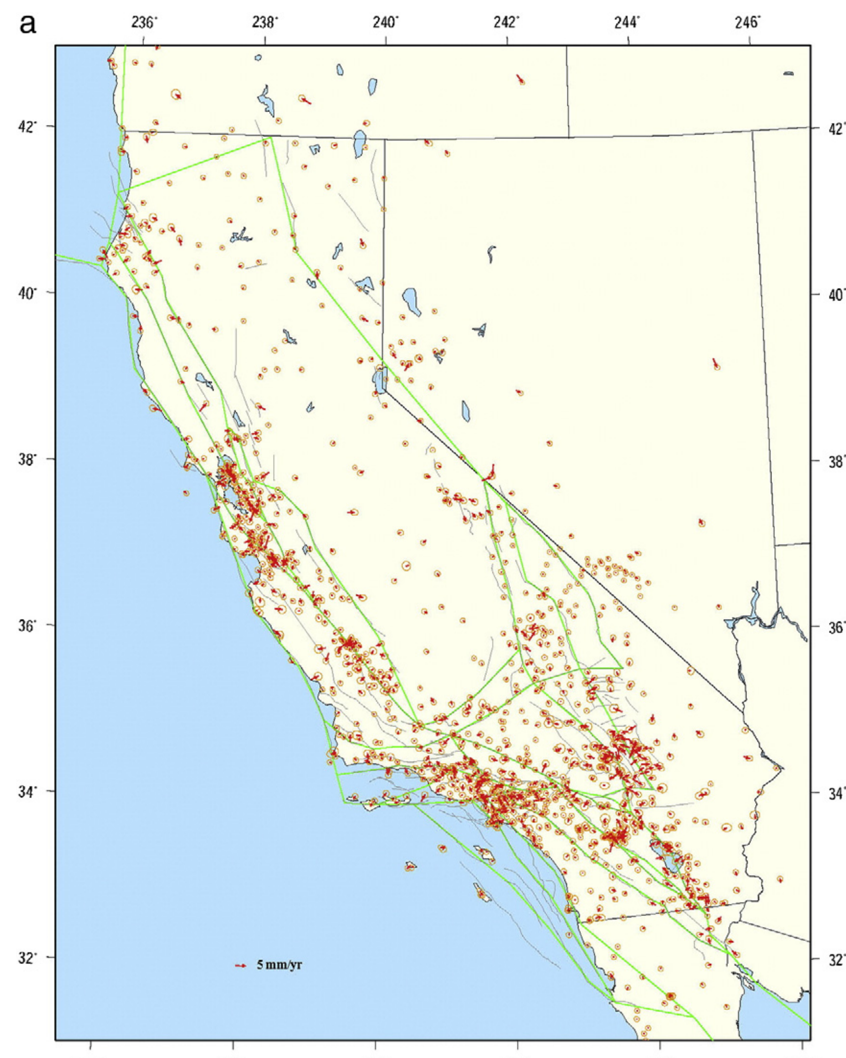

Fig. 8. (a) Residual velocities for inversion using GPS data only. The green lines are the fault network model traces. The residual vectors are plotted in the same scale as the GPS velocities in Fig. 1. The gray traces are faults from USGS quaternary fault database and SCEC UCERF 2 database. (b) Same as (a) but for residual velocities from inversion with geologic slip rate constraints.

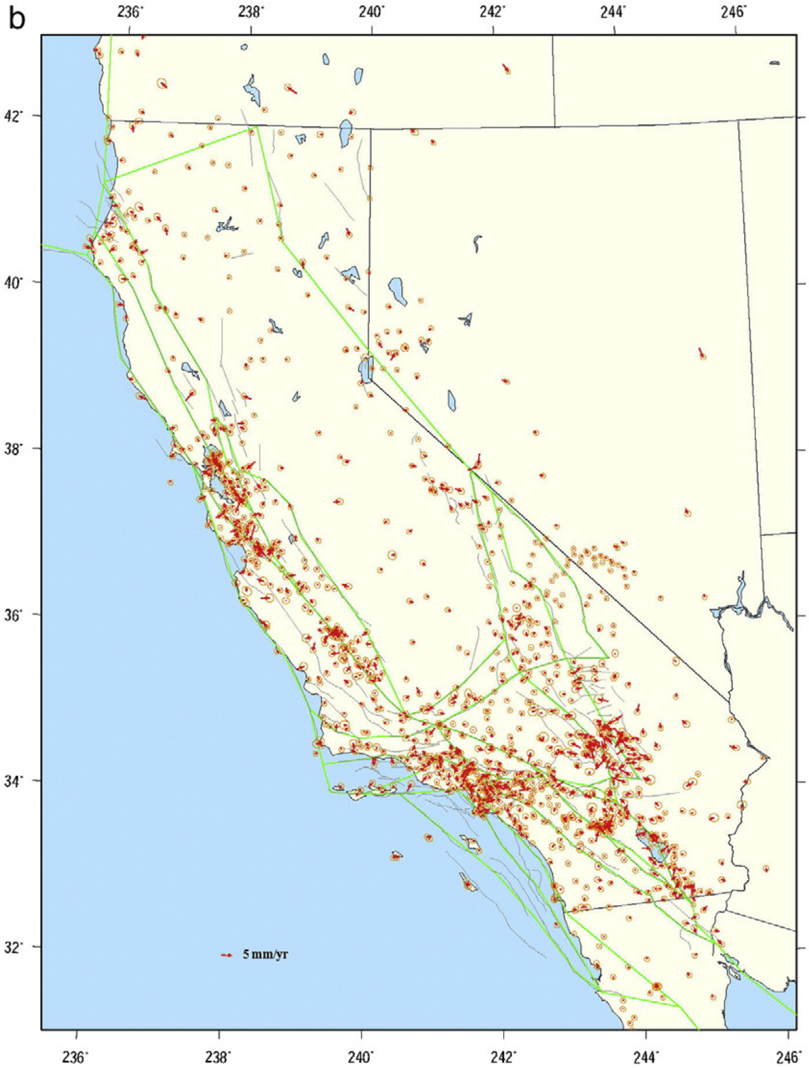

Fig. 8 (*continued*).

For shallow creeps along some of the California faults, rates are essentially the same between inversions with and without geologic slip rate constraints. Along the central California creeping section, we find average creeping rates over the top 5 km vary from 17.1 to 21.5 mm/yr, and from 25.3 to 31.7 mm/yr down deeper. The difference between the top 5 km and below suggests that strain energies accumulated from the partial locking in the shallow portion of the fault are released by episodic creeping events (Rolandone et al., 2008). Elsewhere, shallow creep rates vary from fault to fault. Table 10 lists ranges of the creep rates obtained from our inversions. Our creep results for the Hayward and Calaveras faults are 1.2–5.2 $\pm$ 1.2 and 9–10 $\pm$ 1.6, respectively, significantly lower than that of d'Alessio et al. (2005) (6.5–6.9 mm/yr for Hayward and 12.9–15.0 mm/yr for Calaveras) because of differences in selection of fault lengths and creeping depth. The creeps along the southern Santa Cruz Mountains segment indicate partial locking of the fault segment. The 1989 Mw 6.9 Loma Prieta earthquake ruptured a 70 degree dipping branch of the fault, suggesting that faulting in this area could be complicated, and part of the creeping along the fault segment could be associated with postseismic afterslip.

6. Discussions

One issue in the slip rate inversion using GPS observations is the determination of fault locking depth. With an increase in the locking depth, the slip rate estimates along that fault segment could also increase. This could potentially help resolving the current large discrepancy between GPS slip rates and geologic estimates for the Mojave and San Bernardino Mountains segments of the San Andreas fault since GPS slip rates on those segments are significantly lower than that of the geologic estimates. We have inverted the data to find the optimal locking depths along major faults (A-faults) in California (Working Group on California Earthquake Probabilities, 1995). Since the inversion is nonlinear, we used a grid search algorithm to solve for the optimal depths. We found that there are only marginal improvements (5% or less) to the overall fit of the GPS observations, mostly along the southern San Andreas and Garlock fault segments. Some of those locking depths, such as along the Mojave segment of the San Andreas fault, extended to 25–35 km range (Argus et al., 1999), which is much deeper than the seismogenic depth range for California and extends well into the viscous lower crust layer. We do not know how to interpret the result in a meaningful physical context so we decide to keep the seismicity-based locking depth for all the faults throughout this study.

Fig. 11 shows our preferred strike-slip rate model (Fig. 11a) for California along with the preferred geologic strike-slip rate model (Fig. 11b) from UCERF 2 studies. By comparing slip rates between the two models, we find that there is a significant decrease in slip rates along the San Andreas Fault from the central California through the Mojave to the San Bernardino Mountains segments in our current GPS

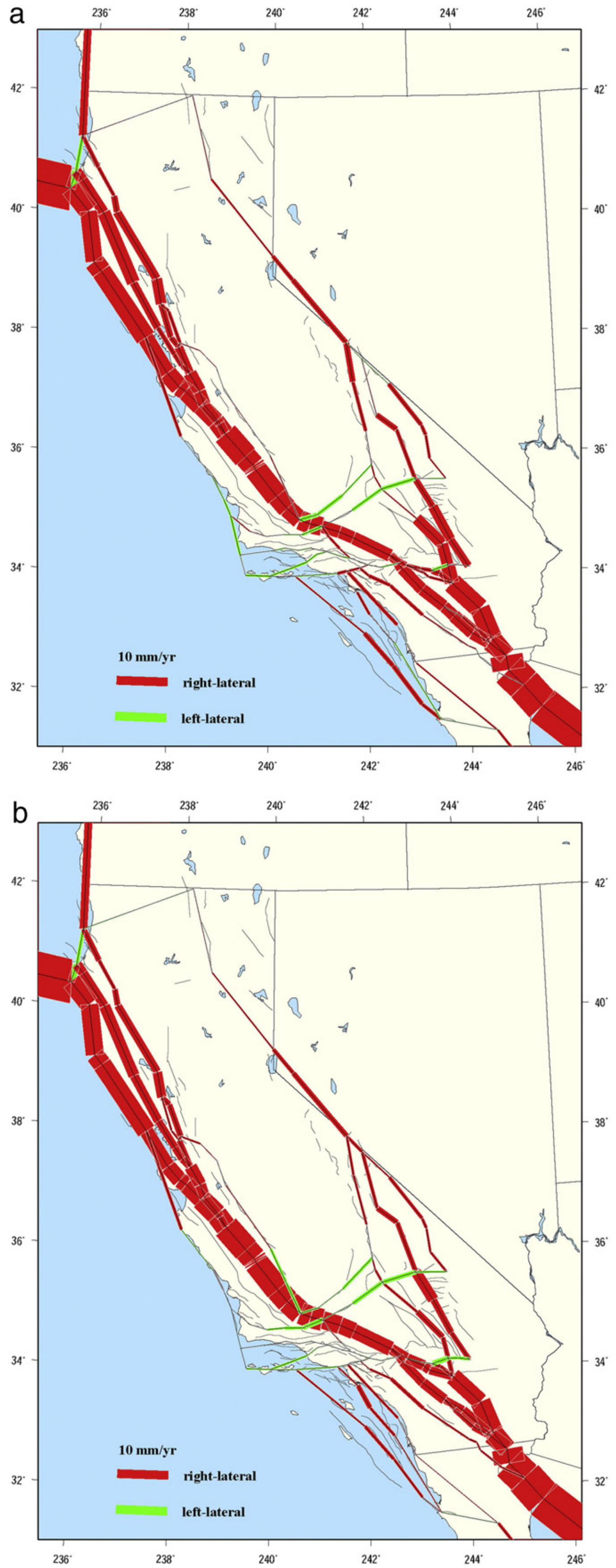

Fig. 9. (a) The strike slip rates determined from inversion without geologic constraints. The red lines are for right-lateral slip and green lines are for left-lateral slip. The width of the lines is proportional to the amount of slip along that fault segment. (b) Same as (a) but for strike slip rates determined from inversion with geologic slip rate constraints.

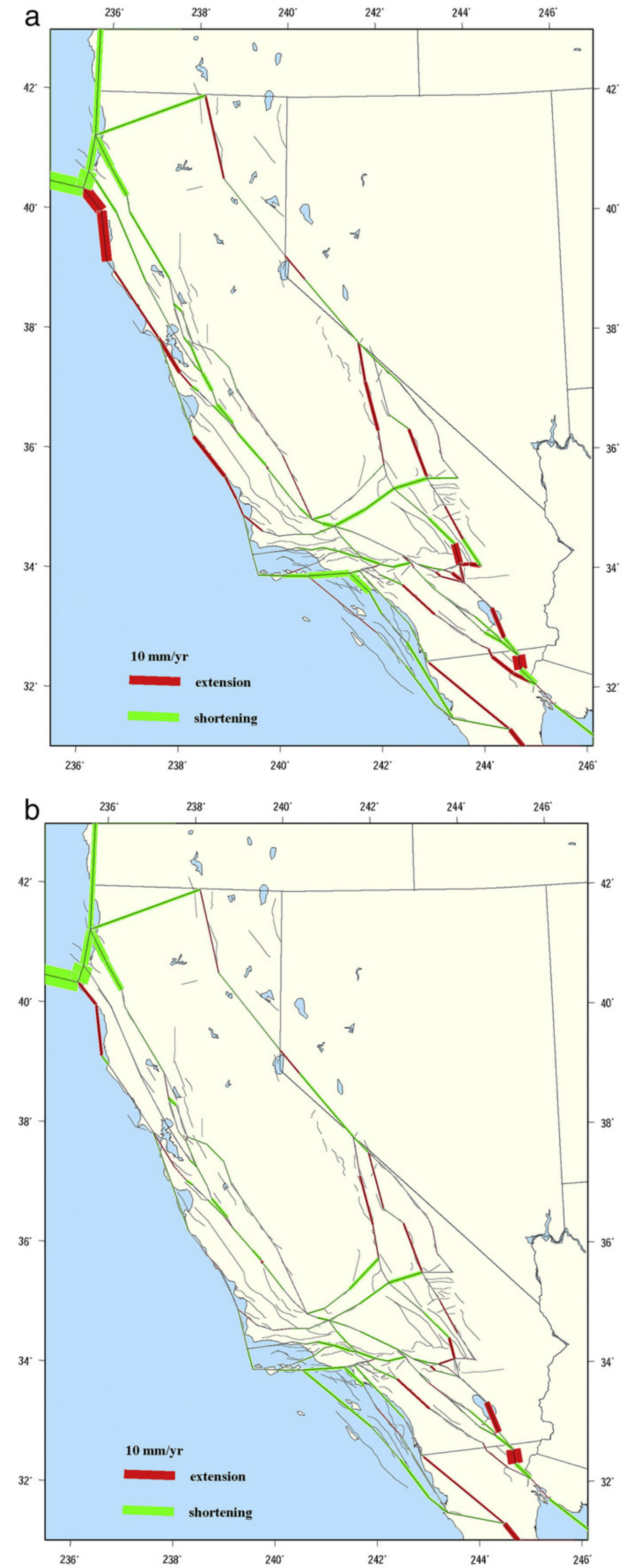

Fig. 10. (a) The dip slip rates determined from inversion without geologic constraints. The red lines are for extension and green lines are for shortening. The width of the lines is proportional to the amount of shortening/extension along that fault segment. (b) Same as (a) but with geologic slip rate constraints.

Table 10
Shallow aseismic creep rates (mm/yr).

4–12 ± 2.0	Northern Parkfield	9.5–9.6 ± 0.7	Southern Santa Cruz Mountains
9–10 ± 1.6	Calaveras	1.2–5.2 ± 1.2	Hayward
0–12 ± 1.6	Paicines	11.0 ± 1.0	Imperial Valley
2.1–2.4 ± 1.2	Brawley	21.5 ± 1.6	SAF Central CA Creeping
		17.1 ± 1.8	SAF San Juan Bartista

inversion solution with geologic constraints. If the geologic slip rates are long-term averages of many cycles of high and low seismic activity periods, our geodetic estimates suggest that the southern San Andreas fault system is currently experiencing a slow tectonic loading time. Consequently a longer recurrence time interval might be expected for a Mw 8 mega-earthquake like the 1857 rupture in southern California. While the southern San Andreas fault may be undergoing a slower period of tectonic loading, the same GPS estimates show a significant increase in slip rates in comparison with the UCERF 2 geologic long-term rates on faults along the Eastern California Shear Zone all the way to the northern Walker Lane, suggesting the region is experiencing a period of faster than average tectonic loading. The recent ruptures of the Landers and Hector Mines earthquakes may be a manifestation of this increased tectonic loading in the Eastern California Shear Zone.

Dolan et al. (2007) found that during the past 12,000 years, there were four bursts of seismic moment release in the Los Angeles region based on paleoseismological observation. These seismically active periods in the Los Angeles region occurred during seismically quiescent periods between similar bursts of seismic activity on the Eastern California Shear Zone. They argued that the observed slip on one system suppresses slip on the other one is a result of a long-range and long-term fault interaction between a system of faults including the Transverse Ranges, Garlock, southern San Andreas, and Eastern California Shear Zone faults. With the Big Bend along the San Andreas Fault as a barrier for the relative motion between the Pacific and North American Plates, we argue that there is a gradual transfer in regional faulting activity from the San Andreas Fault system to the Eastern California Shear Zone and the Walker Lane. While there were alternating periods of seismic activity as a consequence of two fault systems accommodating the same plate-boundary motion, a straight rupture between the two engaging plates will be the ultimate natural result following the least energy principle of physics.

In northern California, we also find a decrease in slip rate along the San Andreas North Coast segment accommodated by an increase in slip rates along the Maacama and Bartlett Springs faults. Similarly, there is also a decrease in slip rate on the San Jacinto fault along the Anza and Clark segments accommodated by an increase in slip rate along the San Gorgonio Pass segment of the San Andreas. These geodetic signals seem to suggest an overall shift in seismic loading in the eastward direction.

Compared to the strike slip motion, the normal slip motion is merely a second order tectonic motion for a major plate boundary system like the San Andreas Fault system in California. However, the normal slip motion is also important for accessing seismic hazard and risk. Recent earthquakes like the 1971 Mw 6.6 San Fernando, 1987 Mw 5.9 Whittier-Narrow, and 1994 Mw 6.7 Northridge earthquakes have demonstrated that blind thrusts in the Los Angeles basin and the Transverse Ranges region could cause major damage to the metropolitan population. Together they have claimed more fatalities than other strike slip events since the 1906 great San Francisco earthquake. Fig. 12 shows our preferred normal-slip rate model (Fig. 12a) for California along with the preferred geologic normal-slip rate model (Fig. 12b) from UCERF 2 studies. Faults highlighted in red are experiencing tensional stress while faults in green are undergoing compressional stress. Although both the geodetic and geologic estimates of the shortening and extensional rates are small, sometimes within its measurement errors, the locations of those shortening and extensional faults from the two models agree well geographically. Right-step bending faults or fault

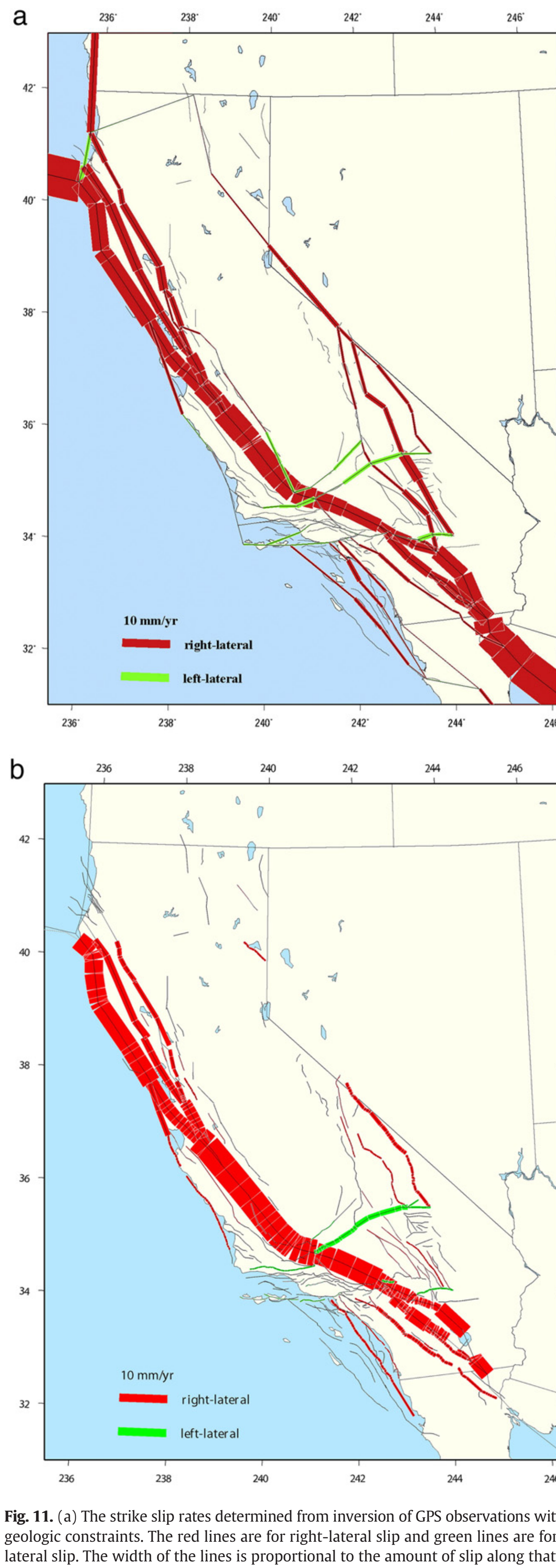

Fig. 11. (a) The strike slip rates determined from inversion of GPS observations with the geologic constraints. The red lines are for right-lateral slip and green lines are for left-lateral slip. The width of the lines is proportional to the amount of slip along that fault segment. (b) Same as (a) but for strike slip rates from UCERF 2 model based mostly on geologic observations.

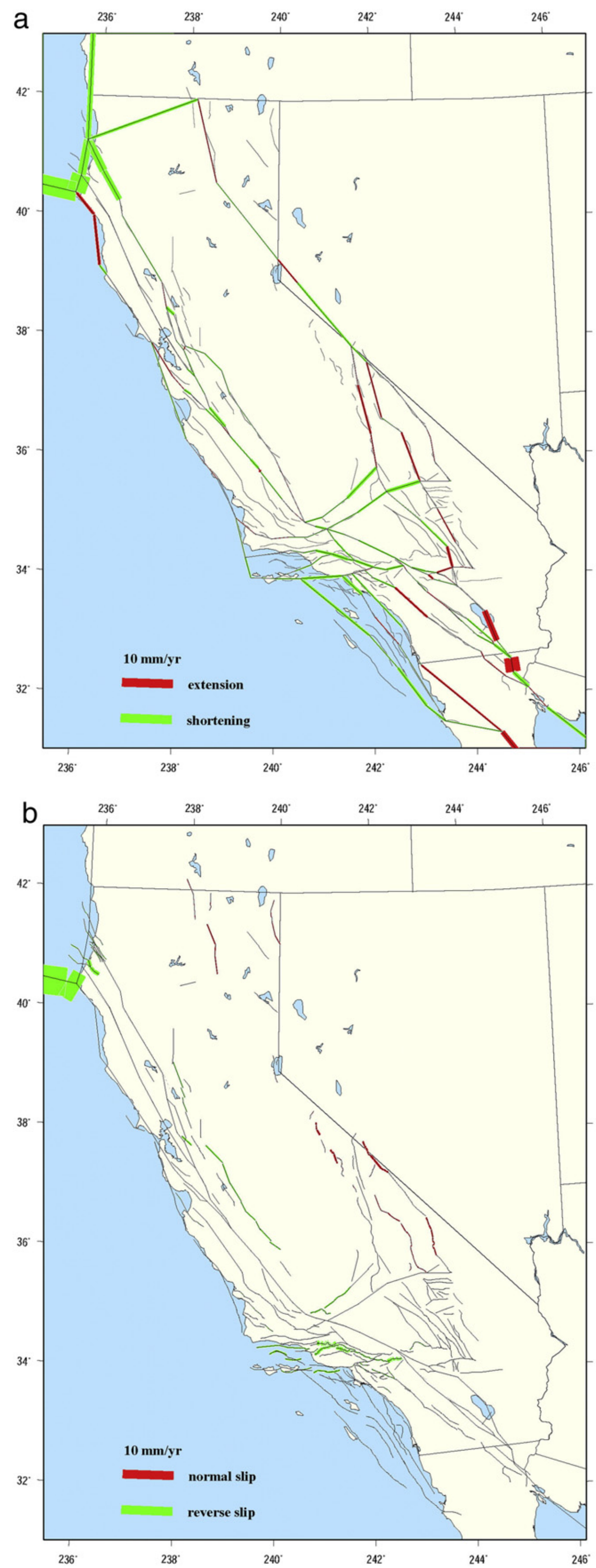

Fig. 12. (a) The fault-nomal slip rates determined from inversion of GPS data with the geologic constraints. The red lines are for extension and green lines are for shortening. The width of the lines is proportional to the amount of shortening/extension along that fault segment. (b) Same as (a) but for rates from UCERF 2 model based mostly on geologic observations.

segments along the major San Andreas slip lines produce releasing bends, for example, the northern San Andreas offshore and the Brawley segment. Right-step oblique faults or fault segments to the major inter-plate strike slip lines along the Walker Lane produce transtensional fault zones, for examples along the Sierra Nevada, Owens Valley and White Mountain faults, the Pisgah, Goldstone, Panamint Valley, and Hunter Mountain faults, and the Death Valley fault system. A left-step fault bending, on the other hand, produces a restraining bend in a right lateral strike-slip fault system. The Big Bend along the San Andreas provides the best example of a major restraining bend that leads to a major compressional uplift for the Transverse Range and crustal thickening of the Los Angeles Basin. This transpressional geologic process extends north to the Garlock and White Wolf fault systems and further south to the off-coast faults along the Palos Verdes fault system and the Santa Cruz-Catalina Ridge and San Diego Trough fault system. Similar results have been found by Meade and Hager (2005) and are consistent with the escape tectonics model in the Los Angeles basin.

Another interesting subject is to examine the geologic and geodetic data for compatibility across active tectonic region. In a system with stable tectonic loading over a period of several seismic cycles, we would expect the geologic slip rates across a fault system be the same as that of the geodetic rates (Savage and Burford, 1973). However, in a complex fault system like California, geologic and geodetic rates differ. Off fault deformation and slip on adjacent fault branches could cause the apparent discrepancy between GPS and geologic estimates, as pointed out by Oskin et al. (2007) in their study of the eastern California shear zone deformation. The discrepancy observed between the two estimates will provide us some insight into the complex interactions in the system or the extent of incompleteness of our deformation model. Figs. 13 and 14 plot the GPS slip rates against the geologic slip rates. The GPS slip rates are obtained from inversions with and without geologic constraints. The geologic slip rates are obtained from the UCERF 2 deformation model. The UCERF 2 geologic rates, even though they are expert consensus rates, depend mostly on geologic field measurements. In some areas geodetic rates and plate rates were considered in developing the USGS quaternary fault model for California (Petersen et al., 1996).

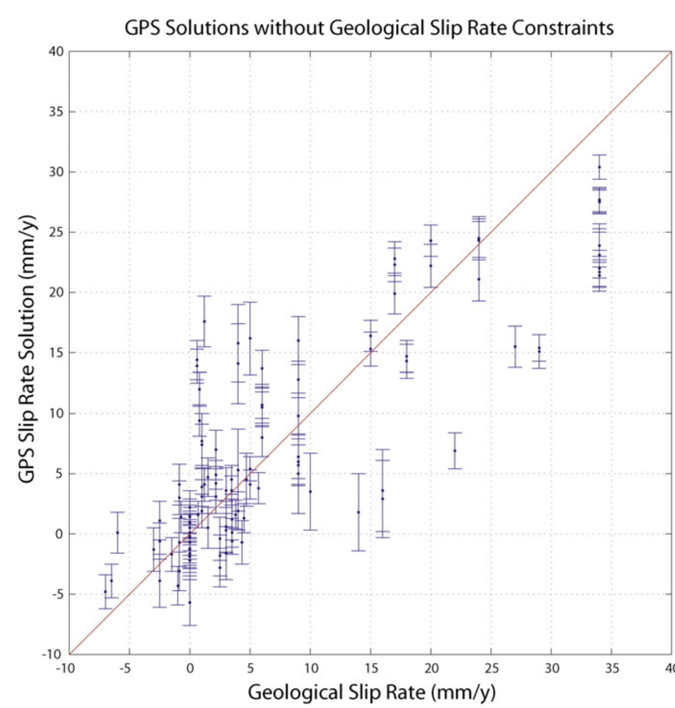

Fig. 13. GPS versus geologic slip rates for California faults. The GPS slip rates are calculated based on inversion without geologic slip rate constraints. The geologic slip rates are from SCEC UCERF 2 model based mostly on geologic observations. Errors are not available for the UCERF 2 geologic slip rates.

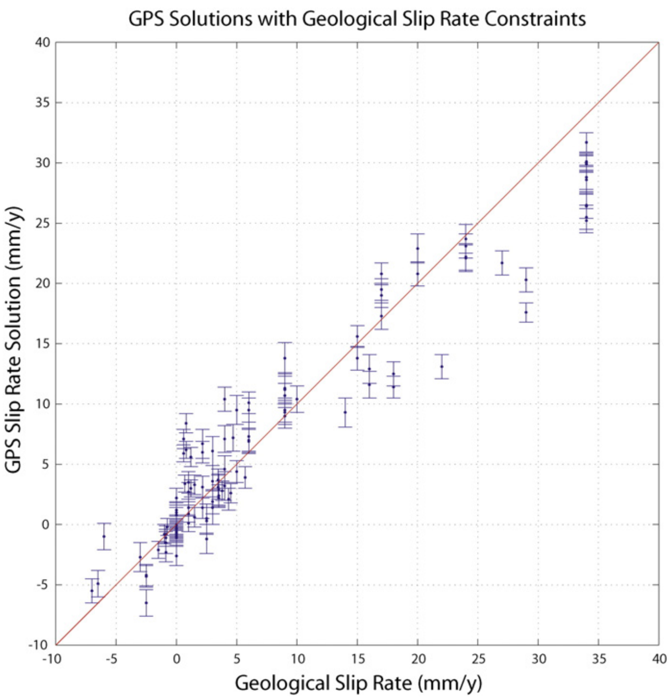

Fig. 14. GPS versus geologic slip rates for California faults. The GPS slip rates are calculated based on inversion with geologic slip rate constraints. The geologic slip rates are from SCEC UCERF 2 model based mostly on geologic observations.

The comparison between the geologic rates and the inverse solution using GPS data only shows large scatter. GPS rates are higher than geologic slip rates mostly on faults in the Eastern California Shear Zone and Walker Lane. GPS rates are lower than geologic slip rates mostly along the central and southern San Andreas, particularly along the Mojave, San Bernardino Mountains and San Gorgonio Pass segments.

Fig. 14 shows a comparison between the geologic and geodetic slip rate estimates with the GPS slip rates constrained by additional geologic information. The agreement between geologic and GPS estimates on slip rates improves significantly when we introduce geologic constraints. The improvement is also expected because of the added geologic slip rate information to constrain the final inverse solution. Weighting of the GPS data and the geologic inputs are the same. The correlation coefficients between the geologic estimates and the model solutions are 0.96 and 0.86 for inversions with and without the geologic constraints, respectively. In statistics, for a correlation coefficient greater than 0.8, the strength of a linear relationship between two variables is generally described as strong. Both model estimates show strong linear dependence with the geologic estimates, suggesting that the geodetic and geologic data are highly compatible for California and its adjacent regions.

Modern GPS observations span only up to 20–30 years. Geologic rates, on the other hand, are long-term average rates typically over several hundreds to thousands of years. By combining the GPS observation with the geologic slip rate data, we assume that the two datasets are compatible or fault slip rates are constant. This may not be a bad assumption in California since most modeled faults are mature faults and the compromise resulted from a constant interseismic slip rate assumption could be minimized. However, a few evolving faults, i.e., under accelerating period of time, could complicate our combined inversion and corrupt the present day fault slip rate. Gourmelen et al. (2011) have studied the Hunter mountain–Panamint Valley fault. They found that their geodetic rate estimate (5.0 ± 0.5 mm/yr) was much faster than that of the geologic average rate (2.3–3.3 mm/yr), suggesting accelerating fault model. Our inversion with and without geologic constraints produces 5.1 ± 0.9 and 2.9 ± 1.2 mm/yr for the Hunter Mountain fault, respectively. Instead of reducing the rate, our UCERF2 geologic constraints (2.5 mm/yr for the Hunter mountain fault) increase the slip rate estimate. A close examination of fault slip rates suggests that the UCERF2 geologic rates on several adjacent faults are significantly lower than that of their geodetic rates. As a consequence, the joint inversion reduces rates on those faults and increases the rate along the Hunter Mountain fault itself as a trade-off between fitting both the GPS velocities and the geologic slip rates. Thus how geologic constraints affect each individual fault is a complicate issue depending on fault network structure and geologic data distribution.

7. Conclusions

With the dense GPS velocity observations becoming available in California and its neighboring states, an accurate estimate of the present day slip rates on major active faults in the region could be obtained. Assuming an elastic half-space model, we studied fault slip rates on major faults in California and its neighbors based on a kinematic fault network model of crustal deformation using GPS observations and geologic constraints.

Based on our F-test result, we find that models with less continuity constraints on slip rate vector across fault nodes fit the data significantly better than the strict block-like model, suggesting significant off fault strain and transient deformation in the study area. It also suggests that the real earth deformation is non-block-like. Our final preferred model is from an inversion of the GPS data with the geologic constraints. In this model, slip rates vary along the San Andreas fault, from around 30 mm/yr in the Parkfield segment to about 19 mm/yr along the Mojave segment and then to about 13 mm/yr along the San Bernardino Mountains segment in southern California; and from 17 to 25 mm/yr along the Santa Cruz Mountain segment, from 9 to 13 mm/yr along the Hayward to Maacama, and from 15 to 3 mm/yr along the central Calaveras to West Napa in northern California, respectively. Slip rates along the Coachella Valley and Brawley segment of the San Andreas are nearly twice of the rates along the San Jacinto fault branch. Unlike the previous studies (e.g., McCaffrey, 2005; Meade and Hager, 2005), slip rates found along the Garlock fault are closely matching with the geologic rates.

Overall slip rates derived from geodetic observations correlate strongly with the geologic slip rates statistically, suggesting geodetic and geologic observations are highly compatible. Nevertheless we find a significant decrease in slip rates along the southern San Andres fault system, and a significant increase in slip rates on faults along the eastern California shear zone up to the northern Walker Lane area compared to that of regional geologic estimates. This implies a significant increase in seismic hazard in the eastern California and northern Walker Lane region, but decreased seismic hazard in the southern San Andreas area at present time than historical average.

We also find depth dependent creeping rates along central California creeping section with rates varying from 15–23 mm/yr over the top 5 km to 21–33 mm/yr underneath. We observe shallow aseismic creep ranging from 4 to 12 mm/yr for the northern Parkfield, southern Santa Cruz Mountain, Hayward, and Calaveras faults. We also find that geodetic derived fault locking depths along major faults in California are quite different from those based on seismicity, but the improvement over their fit to GPS data is insignificant at only 5% or less.

Acknowledgment

We thank Mark Petersen for his comprehensive review of this manuscript. We also thank anonymous reviewers and Editor Rob Grovers for their constructive comments of this manuscript. This research has been partly supported by the Working Group on California Earthquake Probabilities (WGCEP) project through Southern California Earthquake Center (SCEC) and USGS grant G11AP20044.

Appendix A. Supplementary data

Supplementary data to this article can be found online at http://dx.doi.org/10.1016/j.tecto.2013.11.030.

References

Aki, K., Richards, P.G., 1980. Quantitative Seismology: Theory and Methods, vol. 1. W. H. Freeman, San Francisco.

Argus, D.F., Heflin, M.B., Donnellan, A., Webb, F.H., Dong, D., Hurst, K.J., Jefferson, D.C., Lyzenga, G.A., Watkins, M.M., Zumberge, J.F., 1999. Shortening and thickening of metropolitan Los Angeles measured and inferred by using geodesy. Geology 27, 703–706.

Bird, P., 2009. Long-term fault slip rates, distributed deformation rates, and forecast of seismicity in the western United States from joint fitting of community geologic, geodetic, and stress-direction datasets. J. Geophys. Res. Solid Earth 114 (B11), B11403. http://dx.doi.org/10.1029/2009JB0063.

Chuang, R.Y., Johnson, K.M., 2011. Reconciling geologic and geodetic model fault slip-rate discrepancies in southern. Geology 39 (7), 627–630.

d'Alessio, M.A., Johansen, I.A., Bürgmann, R., Schmidt, D.A., Murray, M.H., 2005. Slicing up the San Francisco Bay Area: Block kinematics and fault slip rates from GPS-derived surface velocities. J. Geophys. Res. 110, B06403. http://dx.doi.org/10.1029/2004JB003496.

Dolan, J.F., Bowman, D.D., Sammis, C.G., 2007. Long-range and long-term fault interactions in southern California. Geology 35, 855–858.

Dong, D., Herring, T.A., King, R.W., 1998. Estimating regional deformation from a combination of space and terrestrial geodetic data. J. Geod. 72, 200–214.

Field, E.H., Dawson, T.E., Felzer, K.R., Frankel, A.D., Gupta, V., Jordan, T.H., Parsons, T., Petersen, M.D., Stein, R.S., Weldon, R.J., Wills, C.J., 2009. Uniform California earthquake rupture forecast, Version 2 (UCERF 2). Bull. Seismol. Soc. Am. 99 (4), 2053–2107.

Gourmelen, N., Dixon, T.H., Amelung, F., Schmalzlzle, G., 2011. Acceleration and evolution of faults: an example from the Hunter Mountain–Panamint Valley fault zone, Eastern California. Earth Planet. Sci. Lett. vol. 301 (1–2), 337–344.

Herring, T.A., 2002. *GLOBK: Global Kalman Filter VLBI and GPS analysis program, version 10.0*. (Cambridge: Mass. Inst. of Technol.).

Hammond, W.C., Thatcher, W., 2004. Contemporary tectonic deformation of the Basin and Range province, western United States: 10 years of observation with the Global Positioning System. J. Geophys. Res. 109 (B8), 8403. http://dx.doi.org/10.1029/2003JB002746.

Hauksson, E., 2000. Crustal structure and seismicity distribution adjacent to the Pacific and North America plate boundary in southern California. J. Geophys. Res. 105, 13,875–13,903.

Hearn, E.H., Pollitz, F.F., Thatcher, W.R., Onishi, C.T., 2013. How do “ghost transients” from past earthquakes affect GPS slip rate estimates on southern California faults? Geochem. Geophys. Geosyst. 14 (4), 828–838.

Hill, D.P., Eaton, J.P., Jones, L.M., 1990. Seismicity of the San Andreas fault system: 1980–1986. In: Wallace, R.E. (Ed.), The San Andreas Fault System. U.S. Geological Survey Professional Paper, 1515, pp. 115–152.

Johnson, K.M., Hilley, G.E., Burgmann, R., 2007. Influence of lithosphere viscosity structure on estimates of fault slip rate in the Mojave region of the San Andreas fault system. J. Geophys. Res. 112, B07408. http://dx.doi.org/10.1029/2006JB004842.

King, R.W., Bock, Y., 2006. *Documentation for the GAMIT GPS analysis software, release 10.1*. (Cambridge: Mass. Inst. of Technol.).

Kirby, E., Anandakrishnan, S., Phillips, F., Marrero, S., 2008. Millennial-scale slip rate along the Owens Valley fault, eastern California. Geophys. Res. Lett. 35, L01304. http://dx.doi.org/10.1029/2007GL031970.

LaViolette, J.W., Christenson, G.E., Stepp, J.C., 1980. Quaternary displacement on the western Garlock fault, southern California. In: Fife, D.L., Brown, A.R. (Eds.), Geology and Mineral Wealth of the California Desert. South Coast Geological Society, Santa Ana, California, pp. 449–456.

McCaffrey, R., 2005. Block kinematics of the Pacific/North America plate boundary in the southwestern United States from inversion of GPS, seismological, and geologic data. J. Geophys. Res. 110, B07401. http://dx.doi.org/10.1029/2004JB003307.

McClusky, S.C., Bjornstad, S.C., Hager, B.H., King, R.W., Meade, B.J., Miller, M.M., Monastero, F.C., Souter, B.J., 2001. Present day kinematics of the Eastern California Shear Zone from a geodetically constrained block model. Geophys. Res. Lett. 28, 3339–3372.

McGill, S.F., Sieh, K., 1993. Holocene slip rate of the central Garlock fault in southeastern Searles Valley, California. J. Geophys. Res. 98, 14,217–14,231.

McGill, S.F., Weldon, R.K., Owen, L., 2010. Latest Pleistocene slip rates along the San Bernardino Strand of the San Andreas fault. Geol. Soc. Am. Abstr. Programs 42, 69.

Meade, B.J., Hager, B.H., 2005. Block models of crustal motion in southern California constrained by GPS measurements. J. Geophys. Res. 110, B03403. http://dx.doi.org/10.1029/2004JB003209.

Menke, W., 1989. Geophysical Data Analysis: Discrete Inverse Theory. Academic Press, Inc., New York (revised edition).

Miller, M.M., Johnson, D.P., Dixon, T.H., Dokka, R.K., 2001. Refined kinematics of the Eastern California Shear Zone from GPS observations, 1993–1998. J. Geophys. Res. 106, 2245–2263.

Okada, Y., 1992. Internal deformation due to shear and tensile faults in a half-space. Bull. Seismol. Soc. Am. 82, 1018–1040.

Oskin, M., Perg, L., Blumentritt, D., Mukhopadhyay, S., Iriondo, A., 2007. Slip rate of the Calico fault: implications for geologic versus geodetic rate discrepancy in the eastern California shear zone. J. Geophys. Res. 112, B03402. http://dx.doi.org/10.1029/2006JB004451.

Petersen, M.D., Bryant, W.A., Cramer, C.H., Cao, T., Reichle, M.S., Frankel, A.D., Lienkaemper, J.J., McCrory, P.A., Schwartz, D.P., 1996. Probabilistic seismic hazard assessment for the state of California: California Department of Conservation. Division of Mines and Geology Open-File Report OFR 96–08.

Petersen, M.D., Frankel, A.D., Harmsen, S.C., Mueller, C.S., Haller, K.M., Wheeler, R.L., Wesson, R.L., Zeng, Y., Boyd, O.S., Perkins, D.M., Luco, N., Field, E.H., Wills, C.J., Rukstales, K.S., 2008. Documentation for the 2007 Update of the United States National Seismic Hazard Maps. US Geological Survey Open-file Report 2008–1128.

Pollitz, F.F., Schwartz, D., 2008. Probabilistic seismic hazard in the San Francisco Bay area based on a simplified viscoelastic-cycle model of fault interactions. J. Geophys. Res. 113, B05409. http://dx.doi.org/10.1029/2007JB005227.

Rolandone, F., Burgmann, R., Agnew, D.C., Johanson, I.A., Templeton, D.C., d'Alessio, M.A., Titus, S.J., DeMets, C., Tikoff, B., 2008. Aseismic slip and fault-normal strain along the central creeping section of the San Andreas fault. Geophys. Res. Lett. 35, L14305. http://dx.doi.org/10.1029/2008GL034437.

Savage, J., Burford, R., 1973. Geodetic determination of relative plate motion in central California. J. Geophys. Res. 78, 832–845.

Shen, Z.-K., Jackson, D.D., 2003. Southern California tectonic deformation modeling. 2003 SCEC Annual Technical Report.

Shen, Z.-K., King, R.W., Agnew, D.C., Wang, M., 2006. GPS velocity field for WGCEP. 2006 SCEC Annual Technical Report.

Shen, Z.-K., King, R., Agnew, D., 2011. A unified analysis of crustal motion in Southern California, 1970–2004: the SCEC Crustal Motion Map. J. Geophys. Res. 116, B11402. http://dx.doi.org/10.1029/2011JB008549.

Sieh, K.E., Jahns, R.H., 1984. Holocene activity of the San Andreas fault at Wallace Creek, California. Geol. Soc. Am. Bull. 95, 883–896.

Sims, J.D., 1994. Stream channel offset and abandonment and a 200-year average recurrence interval of earthquakes on the San Andreas fault at Phelan Creeks, Carrizo Plain, California. In: Prentice, C.S., Schwartz, D.P., Yeats, R.S. (Eds.), Proceedings of the workshop on paleoseismology, US Geological Survey Open-File Report 94–568, pp. 170–172.

Weber, G.E., 1994. Late Pleistocene slip rates on the San Gregorio fault zone at Point Año Nuevo, San Mateo County, California. In: Lettis, W.R. (Ed.), Quaternary Transpressional Plate Deformation in the Greater San Francisco Bay Area: Friends of the Pleistocene Pacific Cell 1996 Fall Field Trip, pp. 193–203.

Weldon II, R.J., Sieh, K.E., 1985. Holocene rate of slip and tentative recurrence interval for large earthquakes on the San Andreas fault, Cajon Pass, southern California. Geol. Soc. Am. Bull. 96 (6), 793–812.

Weldon II, R.J., Fumal, T.E., Powers, T.J., Pezzopane, S.K., Scharer, K.M., Hamilton, J.C., 2002. Structure and earthquake offsets on the San Andreas fault at the Wrightwood, California paleoseismic site. Bull. Seism. Soc. Am. 92 (7), 2704–2725.

Weldon II, R.J., Biasi, G.P., Wills, C.J., Dawson, T.E., 2008. Overview of the Southern San Andreas Fault Model. USGS Open File Report 2007-1437E.

Working Group on California Earthquake Probabilities, 1995. Seismic hazards in southern California: probable earthquakes, 1994 to 2024. Bull. Seism. Soc. Am. 85 (2), 379–439.